MOLECULAR DYNAMICS SIMULATION OF THE TRANSPORT PROPERTIES OF MOLTEN TRANSURANIC CHLORIDE SALTS

An Undergraduate Research Scholars Thesis

by

AUSTIN ALAN BATY

Submitted to Honors and Undergraduate Research
Texas A&M University
in partial fulfillment of the requirements for the designation as

UNDERGRADUATE RESEARCH SCHOLAR

Approved by
Research Advisor: Professor Peter McIntyre

May 2013

Major: Physics

Mathematics

TABLE OF CONTENTS

Page

ABSTRACT

Molecular Dynamics Simulation of the Transport Properties of Molten Transuranic Chloride Salts. (May 2013)

Austin Alan Baty
Department of Physics and Astronomy
Department of Mathematics
Texas A&M University

Research Advisor: Professor Peter McIntyre
Department of Physics and Astronomy

The Accelerator Research Laboratory at Texas A&M is proposing a design for accelerator-driven subcritical fission in molten salt (ADSMS), a system that destroys the transuranic elements in used nuclear fuel. The transuranics (TRU) are the most enduring hazard of nuclear power. TRU contain high radiotoxicity and have half-lives of a thousand to a million years. The ADSMS core is fueled by a homogeneous chloride-based molten salt mixture containing $TRUCl_3$ and NaCl. Certain thermodynamic properties are critical to modeling both the neutronics and heat transfer of an ADSMS system. There is a lack of experimental data on the density, heat capacity, electrical and thermal conductivities, and viscosity of $TRUCl_3$ salt systems. Molecular dynamics simulations using a polarizable ion model (PIM) are employed to determine the density and heat capacity of these melts as a function of temperature. Green-Kubo methods are implemented to calculate the electrical conductivity, thermal conductivity, and viscosity of the salt using the outputs of the simulations. Results for pure molten salt systems are compared to experimental data when possible to validate the potentials used. Here I discuss chloride salt systems of interest, their calculated properties, and possible sources of error for our simulations.

DEDICATION

To Jay Atman.

ACKNOWLEDGMENTS

I would like to thank my advisor, Prof. McIntyre, for letting me be a part of the ADSMS project, and allowing me access to his lab. I thank Elizabeth Sooby for her teaching, guidance and advice during this project. The direction and troubleshooting from Prof. Mathieu Salanne and Prof. Paul Madden was also extremely helpful. I acknowledge everyone at the TAMU Accelerator Research Laboratory for creating a very supportive atmosphere to work in. In particular, I want to thank Akhdiiyor Sattarov and Tim Elliott for their help with the computational aspects of this project, Nathaniel Pogue for his work with the COMSOL simulations, and Chase Collins for his help with some of the figures. Finally, I would like to thank my parents and sister for their love, support, and encouragement.

The TAMU Accelerator Research Lab is funded by the Cynthia and George Mitchell Foundation, as well as the Texas ASE fund. My project was partially funded by the Texas A&M office of Honors and Undergraduate Research, through the Undergraduate Research Scholars Program.

NOMENCLATURE

ADSMS	accelerator-driven subcritical fission in molten salt
TRU	transuranics
PIM	polarizable ion model
UNF	used nuclear fuel
MS	molten salt
MeV	Megaelectronvolts
k_{eff}	effective neutron multiplication factor
λ	thermal conductivity
σ	electrical conductivity
η	viscosity
MD	molecular dynamics
RDF	radial distribution function
NVT	canonical ensemble
NPT	isobaric-isothermal ensemble
$g(r)$	radial distribution function
$g_{ij}(r)$	partial radial distribution function
n	number density
N	number of ions in a sample
V	volume
ρ	density

m	mass
C_v	heat capacity at constant volume
U	total internal energy
T	temperature
C_p	heat capacity at constant pressure
H	enthalpy
c_p	specific heat capacity at constant pressure
R	gas constant (8.3144 J K^{-1} mol^{-1})
c	concentration
D	self-diffusion coefficient
ACF	autocorrelation function
$\langle A \rangle$	average quantity of A
k_B	Boltzmann constant (1.3807x10^{-23} J K^{-1})
j_e	microscopic energy current
j_c	microscopic charge current
σ_{xy}	shear component of stress tensor
$V(r)$	potential energy
L_{ab}	Green-Kubo function of the correlation of a and b
$\rho(T)=\beta_d-\alpha_d T$	equation used to fit density temperature dependence
$\sigma(T)=\sigma_0 \exp\left(\frac{E_1}{RT}\right)$	equation used to fit electrical conductivity temperature dependence
$\lambda(T)=\beta_t-\alpha_t T$	equation used to fit thermal conductivity temperature dependence
$\eta(T)=\eta_0 \exp\left(\frac{E_2}{RT}\right)$	equation used to fit viscosity temperature dependence

CHAPTER I

INTRODUCTION

As of April 2012, nuclear power is responsible for producing 13.5% of the world's electricity. 434 commercial reactors operate in 31 different countries, and an additional 150 reactors are either being planned or constructed. In 16 of these 31 countries, nuclear power accounts for 20% or more of national electricity production[1]. However, the benefits of nuclear power do come at a price.

The first major problem with nuclear power is that the fuel cycle is not closed. Used nuclear fuel (UNF) still contains fissile material, isotopes which in theory can still be burned to produce power. Currently this material is wasted because UNF also includes toxic radioactive transuranics (TRU), which have half-lives of hundreds of thousands of years[2]. These hazardous isotopes are problematic when attempting to recycle UNF back into usable fissile material. It *is* possible to remove TRU from UNF, allowing the recycling of fertile materials such as ^{235}U and ^{238}U back into useable nuclear fuel[3,4]. However these processes have not been proven on a large scale, so the nuclear fuel cycle remains open until there is an economic way of returning the fissile inventory locked in UNF to conventional or Gen IV reactors.

Closing the fuel cycle would not solve the radiotoxic waste issue alone. These toxic materials must be sequestered indefinitely in holding ponds on the reactor site in order to prevent an environmental catastrophe or nuclear proliferation. According to the 2012 Blue Ribbon

Commission on America's Nuclear Future, the United States alone currently stores almost 67,000 metric tons and accumulates an additional 2,000 metric tons of used nuclear fuel (UNF) every year[5]. UNF accumulation is also a problem in France, where 74% of the national electrical power comes from nuclear power[1]. A solution to the waste problem would eliminate the largest obstacle currently facing the nuclear industry, and make the production of nuclear power a much more environmentally friendly and sustainable enterprise.

To address this imposing issue, the Accelerator Research Lab at Texas A&M is proposing a design for an accelerator-driven subcritical fission in molten salt (ADSMS) system, a device which utilizes new advances in accelerator technology, neutron spallation targetry, molten salt (MS) chemistry, and materials science engineering. This system is designed to destroy the radioactive waste locked in UNF at the rate at which they are created in a conventional reactor. An illustration of the proposed system can be seen in Figure 1.

The system operates by injecting a beam of protons into an isochronous flux-coupled stack of four cyclotrons, which are able to accelerate the protons to an energy of 800 MeV. Four beams of protons are routed from this accelerator and each beam is split into three smaller beams before being routed to a bank of twelve MS cores. Inside each of these cores is a MS mixture containing dissolved TRU[4]. The proton beams enter these vessels through a beam window and collide with heavy nuclei, shattering them in a process known as spallation. Spallation serves two functions: it destroys heavy nuclei, including TRU, and also produces copious amounts of fast neutrons, coupling the energy from the proton accelerator to the core's fission processes. Fast neutrons having kinetic energy greater than 1 MeV are desired because they fission TRU ten

Figure 1: A representation of the ADSMS system. On the top right, a small cyclotron injects four proton beams into a larger flux-coupled cyclotron. The four resulting beams are then split and injected into twelve molten salt cores containing TRU.

times more frequently than they create it, leading to a considerable reduction in TRU inventory. This is illustrated by the neutron fission and capture cross sections illustrated in Figure 2. When no spallation neutrons are present, each core will have a subcritical effective neutron multiplication factor, k_{eff}, of 0.96. This means that for every 100 neutrons lost by the core, only 96 are produced. The proton beam can be controlled so that the extra spallation neutrons injected into the MS core allow a sustained burning of TRU to occur. If a problem occurs the accelerator producing the proton beams can be turned off. This removes the extra source of spallation neutrons, causing the core's nuclear processes to shrink away without any danger of meltdown.

The use of MS provides a number of safety improvements over conventional reactors. MS has a

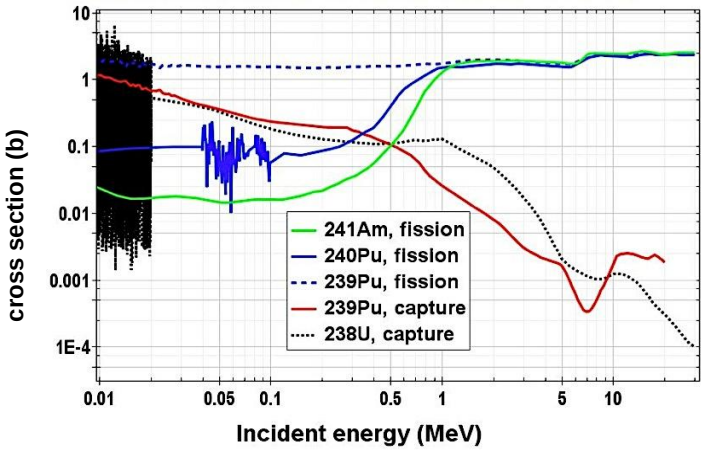

Figure 2: Fission and capture cross sections versus neutron kinetic energy for various transuranics. Neutron capture breeds TRU and is undesireable in this application, whereas fission destroys TRU.[6]

very low vapor pressure at high temperatures, allowing a MS core to operate at standard atmospheric pressure. MS is also chemically inert, drastically decreasing safety concerns. Furthermore, MS exhibits negative thermal reactivity feedback, i.e. k_{eff} decreases when the temperature increases. This is due to MS having a relatively large coefficient of thermal expansion[7,8]. This feedback increases the passive stability of the reactor's k_{eff} value and helps prevent a meltdown.

Lastly, electric power can be produced from this system by harnessing the thermal energy from the cores to run generators. Therefore, this system has many advantages over conventional reactors: it is a safe subcritical system, it can run on UNF, taking advantage of the fissile material remaining in UNF, and it destroys many long-lived waste isotopes[9].

This device can also be reconfigured to be a TRU isobreeder instead of a burner, enabling it to convert ^{238}U into ^{239}Pu at the same rate that ^{239}Pu is burned. This would remove the need to

periodically replenish each core's TRU inventory to sustain power production. The core would be self-sustaining, consuming fertile ^{238}U without creating new TRU. The isobreeder is therefore an option for closing the nuclear fuel cycle.

Motivation

In order to model such a device, it is of vital importance that the properties of the MS fuel are well understood. For example, a higher fuel density correlates to more mass being present in the volume permeated by the proton beam, increasing the efficiency of the spallation process. By similar logic a larger density also raises the neutron flux, and thus the k_{eff} of the core. It follows that a complete understanding of the temperature dependence of the fuel density will make controlling the core criticality possible. The heat capacity of the MS relates a system's energy and its temperature. In our system energy is input by a proton beam of fluctuating power, leading to fluctuations in the core's MS temperature which in turn causes changes in the core's thermal energy output based on the fuel MS's heat capacity. A melt's thermal conductivity, or λ, indicates how rapidly it transfers heat across a temperature gradient. This property and the heat

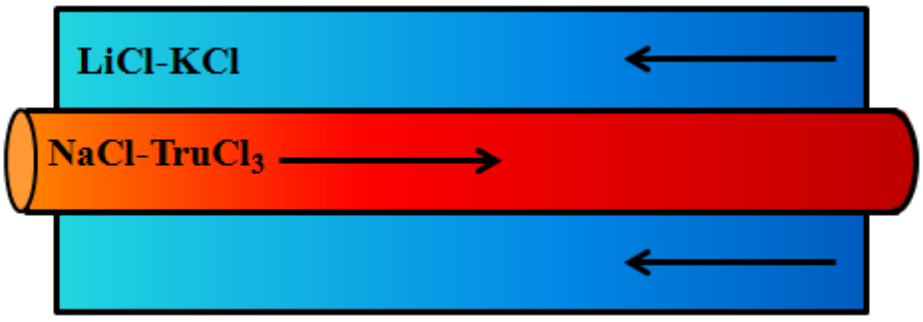

Figure 3: Schematic diagram of an ADSMS counterflow heat exchanger. Hot fuel salt runs through a Ni pipe immersed in a circulating bath of LiCl-KCl eutectic salt. The two salts flow in the opposite directions to optimize heat transfer.

capacity are important attributes when constructing and evaluating the efficiency of a core's cooling systems[10].

In order to illustrate this, simulations of a proposed ADSMS counterflow heat exchanger were performed in COMSOL Multiphysics[11]. A simple diagram depicting the basic design of this heat exchange can be seen in Figure 3. Heat is transferred from the fuel salt through a nickel intermediary into a colder secondary MS. The simulation was repeated using slightly increased values for the fuel's heat capacity and λ. These results have been plotted in Figure 4. A larger fuel salt heat capacity increases the temperature in the heat exchanger because more energy transfer is required in order to lower the salt temperature by the same exchanger more effective at cooling the fuel salt. Despite the different behaviors in MS temperature, both of these changes

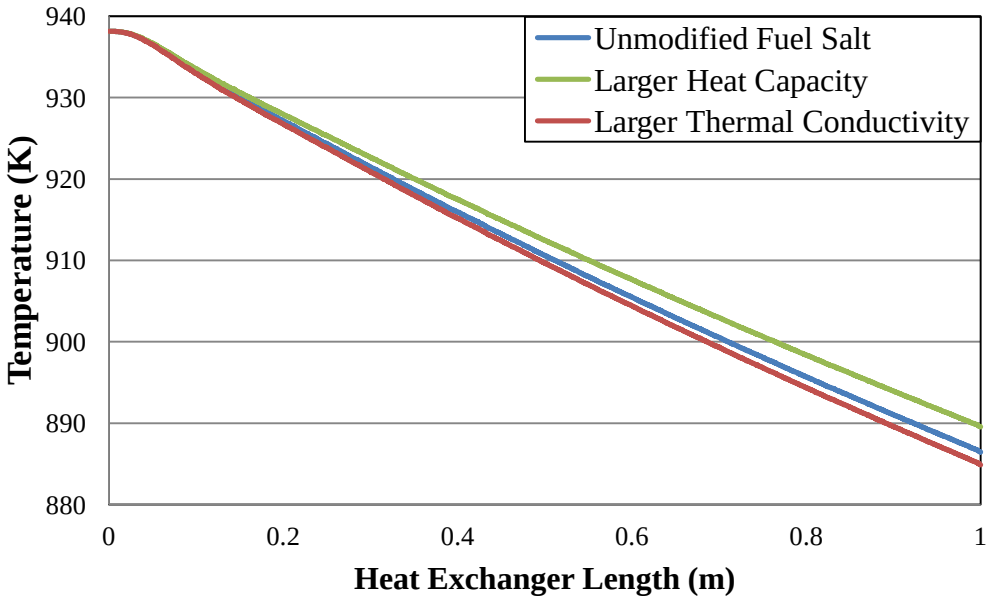

Figure 4: COMSOL simulations of fuel salt temperature versus heat exchanger length. The thermal properties of the fuel salt are each increased by 10% to demonstrate their effect on the heat exchanger.

increased the efficiency of the heat exchanger by about 3%. The property of electrical conductivity, σ, is similar to λ in that it dictates how much current will flow in a MS due to an electric potential gradient. Thermal and electrical conductivities are physically related in this system, since the movements of ions cause electrical current as well as heat transfer. As a consequence the two conductivities can usually be calculated simultaneously. (Electrical conductivities are an important property in fuel cell technologies.) Finally, the system's viscosity, η, quantifies the relationship between the speed of MS flow and the shear acting on the salt due to friction from pipes. Viscosity usually has strong temperature dependence, and the pumps and pipes in each core must be chosen with the salt's viscosity in mind to ensure adequate fluid circulation.

The computational tool used in this study is a Molecular Dynamics (MD) program. This code takes an input data file that characterizes a sample of MS by specifying the type, position, and velocity of a few hundred ions. A visualization of the contents of this input file can be seen in Figure 5. Additional input files define other parameters such as the temperature, pressure, and time-step, which affect the computational experiment. After the inputs are initialized, the program calculates the force on each ion, allowing it to solve the equation of motion at each time step in the simulation[12]. In order to calculate these forces, the program uses a polarizable ion model (PIM) employing an ionic interaction potential which is able to account for short range electrostatic, dispersion, and particle repulsion forces, as well as ion polarizations due to long range interactions[13]. Use of this model is crucial to obtaining physically permissible results, as molten salts are highly polarized. The equations of motion are then used to acquire the volume, stress tensor, energy, dispersion factors, and dipoles of the ionic assembly. With this information

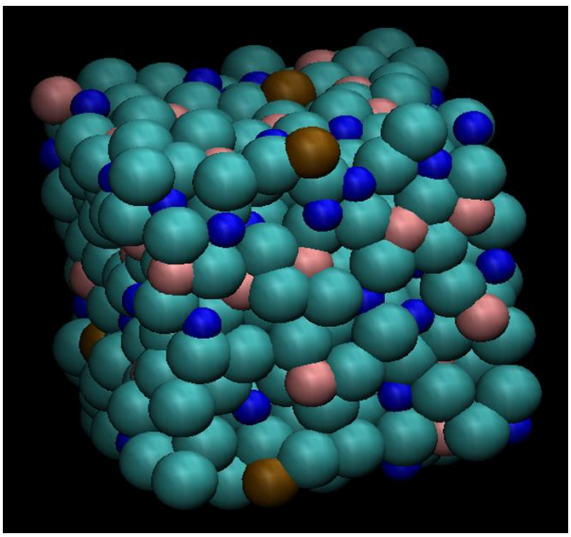

Figure 5: Visualization of a typical molecular dynamics cell. The disordered and closely packed Cl^- (teal), Na^+ (blue), U^{3+} (pink), and Pu^{3+} (brown) ions indicate that the system is in liquid phase.

statistical mechanics and Green-Kubo relations can be used to compute the properties of large collections of ions, including their density, heat capacity and transport properties. In this way a library of melt properties based on melt composition can be constructed.

We begin with simulations of well-studied pure compounds, such as sodium chloride, in order to verify that they behave in the correct physical manner. To do this we calculate the radial distribution functions (RDF) of the liquid. The simulated MS has the correct atomic structure if the RDFs match data taken by X-Ray diffraction experiments. This means the results of our simulations are firmly based in experiment[12], and we then move on to simulating mixtures of these compounds. We are specifically interested in mixtures of the ions $Pu^{3+,}$ U^{3+}, La^{3+},Na^+, Li^+, K^+, and Cl^- because of their potential use in an ADSMS system.

CHAPTER II

THERMODYNAMICS AND STATISTICAL MECHANICS

There is over 2.5 metric tons of MS contained within one ADSMS core, corresponding to over 10^{28} ions - a number 10,000 times larger than the estimated number of stars in the observable universe. This presents us with a dilemma; we wish to predict the thermodynamic behavior of our core, but it contains an intractably complex system of MS. Complicating the issue is the fact that there is little experimental data on the fuel salt composition. We can alleviate these problems by shrinking our view down to the microscopic scale and looking at only a few hundred ions. Firstly this decreases the computational time required to model the system. The time required to calculate a MD model is proportional of the number of ions squared, so reducing from 10^{28} ions to 10^{3} ions changes the required time from eons to a few hours or days. Secondly, there is more data concerning how molten salts interact at a microscopic level, allowing us to base our model on real physical parameters.

Here we develop the tools required to link our small microscopic MD simulations to the properties measured in macroscopic samples of MS. The concept of a thermodynamic ensemble allows us to relate two macroscopically identical but microscopically different systems. Radial distribution functions can be used to relate our microscopic model to experimental data on the atomic structure of MS samples. Finally, we describe the macroscopic properties we are interested in modeling, and develop Green-Kubo relations allowing us to calculate them from information calculated in our microscopic models.

Thermodynamic ensembles

An ensemble is a collection of systems which share certain macroscopic properties regardless of their microscopic state. As an example, consider two samples containing a gram of NaCl salt held at a constant temperature and volume. Both of these samples are members of the same ensemble, even though the individual positions of each ion in the sample may differ greatly. Because of this we expect to measure the same values for all macroscopic properties in these samples and any other one gram samples of NaCl held at the specified volume and temperature. The notion of an ensemble is therefore an important tool needed for generalizing results calculated from one specific microscopic configuration of MS. There are three thermodynamic ensembles of particular importance for working with MS: the microcanonical, canonical, and isobaric-isothermal ensembles.

In conventional MD simulations the system is completely isolated, so its total energy is a constant of motion[12]. This makes the microcanonical, or NVE, the ensemble around which MD is built. Systems in this ensemble contain the same number of particles, have the same volume, and have a specified total energy. Unfortunately the NVE ensemble does not recreate a laboratory setting; a real system cannot be completely energetically isolated from its surroundings to prevent energy transfer.

If we postulate that the system is able to exchange energy with a large external heat sink, then the energy of the system may fluctuate but its temperature will not. This creates the canonical, or NVT, ensemble which has a constant volume, temperature, and number of particles. This ensemble is particularly useful because it allows for the calculation of the system's transport

properties. While the canonical ensemble is mathematically useful, it still does not reflect the conditions used in most modern experiments.

The isobaric-isothermal, or NPT, ensemble is usually the most applicable ensemble for experimenters. Here the system has a constant number of particles and is kept at constant pressure and temperature. Temperature and pressure can be easily monitored and controlled by simple thermometers, pressure gauges and heating elements. Another advantage of the NPT ensemble is that it does not constrain the volume of the system, making it more useful for calculating the temperature dependence of a MS's density.

One of the main arguments for using MSs in a nuclear system has to do with their low vapor pressures. This allows the salt to be heated to extremely high temperatures without increasing the pressure inside the core of the system. As a consequence, modeling a system using the isobaric-isothermal ensemble is very close to reality for this application, making it our preferred ensemble. However, some of the methods developed in this paper concerning transport properties employ the canonical ensemble. If this ensemble is used, the constrained volume is taken to be the equilibrium value from a previous isobaric-isothermal calculation.

Radial distribution functions

Some of the simulations done in this study require as many as 100 input parameters to be specified before the calculation begins. It is therefore possible to have a bad combination of inputs cause the model to converge to a solution not reflecting a realistic system. An example of this can be seen in Figure 6. The left group of ions has a structure that is too diffuse for a real

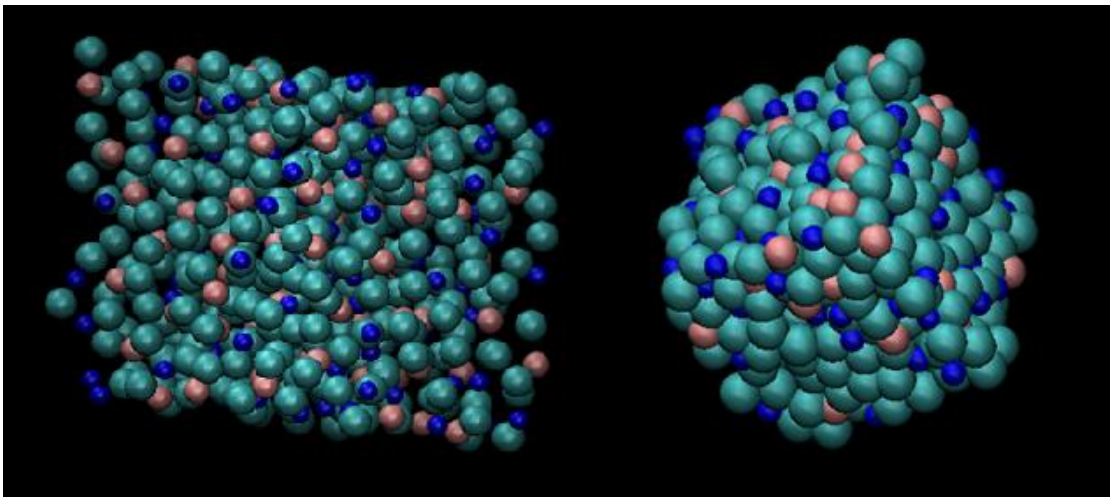

Figure 6: Two models of the same MS having different microscopic structure. The left group is too diffuse to represent a real sample of MS, and its RDF would not correlate with experiment. The right group is a more realistic model.

MS, which should look like the tightly packed group on the right. It is of primary importance to prove that a simulated MS system has the same microscopic structure as a real sample of MS. This will show that the salt is behaving realistically at the microscopic level, which in turn indicates that the macroscopic properties that result from this microscopic behavior are also realistic.

In order to quantify the microscopic structure of the MS, we calculate its RDF, g(r). This function is defined as

$$g(r)=\frac{n(r)}{n}, \qquad (1)$$

where n is the average number density, N/V, of the salt, and n(r) is the *local* number density of the salt at a distance **r** away from some reference particle. The RDF describes as MS's local configuration by representing where its constituent ions are in relation to each other. For an

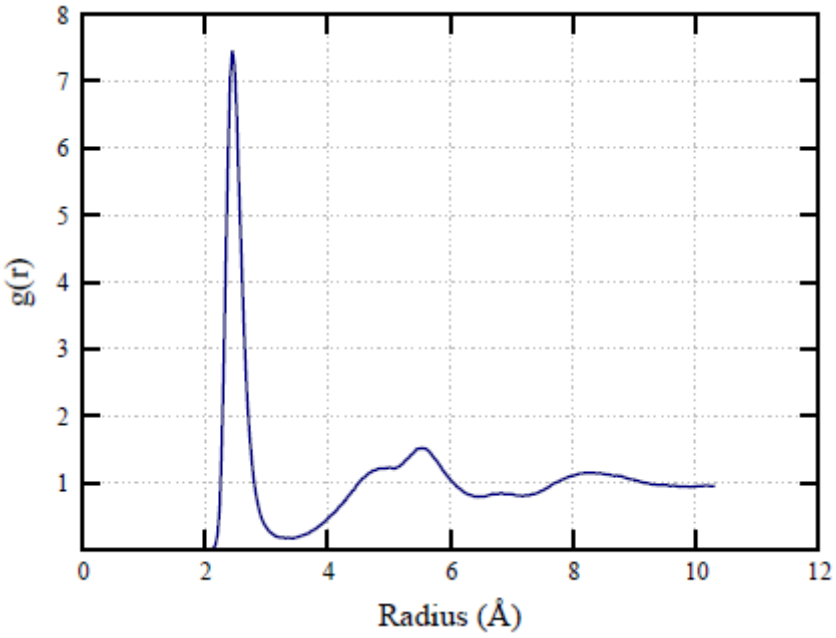

Figure 7: A typical molten salt RDF. The large first peak indicates large interactions between neighboring ions. As the distance between ions increases, the strength of interaction decreases and g(r) converges towards unity.

ideal gas that has no intermolecular forces, $g(r)=1$. Deviations from unity are large in ionic liquids because of the strong dispersion and polarization forces present. A typical molten salt RDF is shown in Figure 7. The RDFs of many molten salts have been measured experimentally using neutron and X-ray diffraction techniques, allowing us to benchmark how well our simulations reproduce molten salt systems. It should be noted that this technique is not new, and has been used in many previous MD studies[14,15].

Density

The density, ρ, of a system is defined as the ratio of its mass to volume,

$$\rho=\frac{m}{V}. \qquad (2)$$

This makes a MS's density one of the easiest properties to calculate. In general a system's volume, and therefore its density, is a function of the temperature. For MS an increase in temperature leads to a linear decline in density, meaning a simple linear regression is adequate for modeling the temperature dependence of this property. The density of a MS is of critical importance when calculating the neutronic behavior of a nuclear system. Spallation neutron sources, such as SNS at Oakridge National Laboratory, use very dense heavy metal spallation targets to produce several neutrons from a single proton. Using the same reasoning, a high salt density increases the effectiveness of the salt as a spallation target for incident protons, leading to significant neutron production. Thus, if a salt is too dense the system can become more prone to criticality. However, if a salt is not dense enough, the mass of fuel that can be fit into a given space will be too small to sustain long-term operation of the device. Finally, the thermal dependence of a salt's density must be known in order to determine the device's thermal reactivity feedback coefficient. Essentially, an increase in temperature of the system will increase its criticality. However, an increase in temperature also leads to a decrease in MS density, which lowers criticality. Because of this, a larger temperature dependence leads to greater neutronic stability in the system, increasing safety.

Heat capacities

A system's heat capacity is a measure of how much energy is required to change its temperature. Mathematically for a system at constant volume, we write the heat capacity at constant volume as

$$C_V = \left(\frac{\partial U}{\partial T}\right)_V \tag{3}$$

where U is the system's total internal energy. As stated earlier experiments are rarely carried out at constant volume, as a constant pressure environment is easier to obtain. It is therefore more convenient to define the heat capacity at constant *pressure* by adding in a PV term to account for work done during volumetric expansion[16].

$$C_P = \left(\frac{\partial(U+PV)}{\partial T}\right)_P = \left(\frac{\partial H}{\partial T}\right)_P \quad (4)$$

Here we have introduced the symbol H to represent the U+PV term, which is commonly called the system's enthalpy. For MS C_p is usually very close to C_v, and has very little temperature dependence.

It should be noted that the heat capacity of a system depends on its size; a large sample of MS will take more energy to heat by the same amount as a small one. In order to resolve this, we divide the heat capacity by the system's total mass in order to form a parameter that only depends on the type of MS in the system. This molten salt property is referred to as specific heat capacity and is denoted with a lowercase c,

$$c_p = \frac{C_p}{m}. \quad (5)$$

In this study, both the temperature dependence of a MS's density and its c_p value are calculated using the NPT ensemble.

Calculation of a nuclear core's heat capacity is required in order to appropriately design heat transfer systems for the device. As seen earlier, a larger fuel salt heat capacity will decrease the ability of the core's heat exchangers to cool the system. Additionally, a larger heat capacity will cause the core temperature to be more stable when subject to fluctuations in power due to the

incident proton beam. Finally, the heat capacity is an important factor used for evaluating many emergency scenarios. For example, if the core's heat exchangers failed, the rate of the device's temperature increase would be a function of its heat capacity.

Transport properties

The set of parameters describing the dynamics of mass, charge, and energy flow within a material are collectively referred to as transport properties. In this study we examine three major transport properties: the thermal conductivity, electrical conductivity, and shear viscosity.

The thermal conductivity, λ, of a substance is a measure of how much heat will flow in a material due to a temperature difference. It is the proportionality constant in Fourier's law of heat conduction[16]:

$$\vec{q} = -\lambda \nabla T. \qquad (6)$$

Here $\vec{q}$ is the heat flux density, which accounts for how much energy flows through a surface in the system. In MS systems λ itself has a weak temperature dependence.

Knowledge of a MS's λ is of vital importance when designing coolant systems. We have shown that a larger λ increases the cooling effect of heat exchangers, but a low λ can cause cooling systems or energy inputs to engender large temperature gradients within the MS. These gradients can lead to nonuniformities in the criticality and power production in the core. In general, high thermal conductivities are desirable for this application, as they help keep the core temperature more isotropic.

Electrical conductivity, σ, is an analogue of λ describing how electric current responds to electric fields. It is found in Ohm's Law relating the current density, $\vec{j}$, to electric potential, ϕ.

$$\vec{j}=-\sigma\nabla\phi \tag{7}$$

In general, λ and σ are intimately related in MS systems, since the ions transferring heat are also the charges producing current in the system. This means that these quantities can be calculated together in certain cases.

Finally, the shear viscosity, η, of a system relates stress then strain rate experienced by a material due to forces between its constituent particles. If τ is the stress experienced by a system, then a shear rate, $\partial u/\partial x$, will occur according to the relation[16],

$$\tau=\eta\frac{\partial u}{\partial x}. \tag{8}$$

Liquids with higher viscosities are thicker, flowing less easily and requiring more force to pump through pipes. The viscosity of a liquid usually has notable temperature dependence, given in the Arrhenius model as

$$\eta=\eta_0\exp\left(\frac{E_2}{RT}\right). \tag{9}$$

Here η_0 and E are constants that can be determined empirically, and R is the ideal gas constant. We mention that σ also has a temperature dependence of this form, but it is usually much weaker and has a negative E value.

We are interested in MS viscosity because it dictates what types of pipes and pumps must be used when circulating the fuel salt through the core and its heat exchangers. If the core's pumps are underpowered for a thick MS, the heat exchangers will not receive enough fluid flow keep

the entire system cooled. Additionally, the spallation window is cooled by a flow of incident molten salt, and may crack if the salt flow is insufficient. Therefore, the pumps must be powerful enough to supply adequate circulation to the core for the range of viscosities determined by the temperature dependence of the molten salt.

Green-Kubo relations

Molecular dynamics simulations do not readily calculate the transport properties of MS. Instead, they output the positions and velocities of individual ions in the melt. In order to calculate the transport properties from this information, we must use so-called Green-Kubo relations. To develop these relations, we will consider the diffusion of particles in a one-component ionic liquid. This liquid will have a concentration profile given by c(r,t) and a particle flux J. Diffusion in this liquid is described by Fick's first law, and has a corresponding transport property, the self-diffusion coefficient D.

$$J=-D\nabla c \tag{10}$$

Furthermore, the number of particles is conserved, so we can also write

$$\frac{\partial c}{\partial t}=-\nabla\cdot J. \tag{11}$$

Combining these two equations yields the differential equation[17]

$$\frac{\partial c}{\partial t}=D\nabla^2 c. \tag{12}$$

If we assume c is normalized to unity, we can multiply both sides by r^2 and integrate over three dimensional space, yielding

$$\frac{\partial}{\partial t}\int r^2 c(r,t)dV=\frac{\partial\langle r^2(t)\rangle}{\partial t}=6D. \tag{13}$$

Here we adopt the convention that triangle brackets refer to the average of whatever quantity they contain. The 6 on the right hand side is a result of integrating by parts on the Laplace operator acting on c. We now note that a particle's position is the time integral of its velocity, so

$$\frac{\partial\langle r^2(t)\rangle}{\partial t}=\frac{\partial}{\partial t}\langle\left(\int_0^t v(t')dt'\right)^2\rangle=\frac{\partial}{\partial t}2\int_0^t dt'\int_0^{t'}dt''\langle v(t')\cdot v(t'')\rangle. \qquad (14)$$

By substituting (14) into (13) and evaluating the time derivative with the first integral, we obtain[17]

$$D=\frac{1}{3}\int_0^t dt''\langle v(t)\cdot v(t'')\rangle. \qquad (15)$$

At this point, it is convenient to redefine the time origin so that $t''=0$ and $\tau=t''-t$. This can be done because the behavior of our system is invariant under translations in the time coordinate. The resulting argument of the integral, $\langle v(\tau)\cdot v(0)\rangle$, is known as the velocity autocorrelation function (ACF). Its value starts at 3 (for 3 dimensions) and will eventually converge to zero as $\tau\to\infty$. When we let the upper limit of the integral go to infinity, the value of D should converge:

$$D=\frac{1}{3}\int_0^\infty d\tau\langle v(\tau)\cdot v(0)\rangle. \qquad (16)$$

Relations such as this one, between transport properties and integrated autocorrelation functions, are broadly referred to as Green-Kubo relations. They are useful in molecular dynamics simulation because the autocorrelation function can readily be calculated from the output of a MD code.

It should be noted that the equations containing the three transport properties we are interested in have a form close to that of (10). Furthermore, these transport properties describe the motion of conserved quantities, so (11) is also fulfilled. Not surprisingly, solutions to these equations

having Green-Kubo form exist. The λ of a system can be related to its energy current, j_e, with the relation

$$\lambda = \frac{1}{3k_B VT^2}\int_0^\infty d\tau \langle j_e(\tau)\cdot j_e(0)\rangle. \quad (17)$$

For electrical conductivity, the charge current, j_c, is used to give the equation

$$\sigma = \frac{1}{3k_B VT}\int_0^\infty d\tau \langle j_c(\tau)\cdot j_c(0)\rangle. \quad (18)$$

Finally, to determine the viscosity of a system the shear components, σ_{xy}, of the stress tensor are contained in the autocorrelation function[12,17]

$$\eta = \frac{1}{k_B VT}\int_0^\infty d\tau \langle \sigma_{xy}(\tau)\sigma_{xy}(0)\rangle. \quad (19)$$

It should be remembered that these formula are for a one-component ionic liquid, and are therefore inappropriate for calculating the transport properties of more complicated MSs. Luckily, they can be expanded upon using the Onsager reciprocal relations in order to be appropriate for multi-component systems[18]. See Appendix A for a detailed description of the formula used for these types of systems.

CHAPTER III

MOLECULAR DYNAMICS METHODS

There exist two favored methods for modeling properties of molecular systems: Molecular Dynamics and the Monte Carlo method. Of these two methods, MD simulation is better for measuring dynamic properties because it specifically calculates the equations of motion for each particle in the simulation. It is therefore natural to choose MD for calculating transport properties of molten salt systems.

Fundamentally MD consists of three steps: initialization, force calculation, and integrating the equations of motion[12]. During initialization the location of each ion in the simulation, as well as other parameters such as temperature, are specified. This phase also allows the ion velocities be either specified by the user, or generated to fit an appropriate thermal energy distribution. Using this data and a set of user-specified interaction potential parameters, the code calculates the potential energy, V(r), of each ion due to every other ion. From this information the net force on each ion is calculated. Finally, the code uses these forces to extrapolate the positions and velocities of each ion after a very small time step on the order of 1 fs. The last two steps are then repeated for as long as desired in order to fully describe the equation of motion for each ion. We expect a properly working code to give physically relevant solutions for any input temperature or ion configuration. Therefore special attention should be paid to the interaction potential parameters, as they are the main determining factor as to whether the code's output solutions are physically relevant.

Interaction potentials

Most conventional MD codes are not suited for simulating ionic liquids because complex long-range forces due to the ions polarizing each other are not accounted, leading to nonphysical results. We therefore use a MD code developed by Madden and Wilson[19,20] which is specifically calculates these polarization effects as well as repulsion, dispersion and Coulombic effects. The interaction potentials in this code are divided into two types: short and long range interactions.

The short range interactions include ionic repulsion due to ions not wanting to occupy the same space, and dispersion forces caused by ions inducing multipoles in the electric structure of their neighbors. The interaction between the ith and jth ion in a system are described by a pair potential having Born-Mayer form[21]:

$$V(r_{ij}) = B^{ij} e^{-a^{ij} r_{ij}} - f_{ij}^{(6)}(r_{ij}) \frac{C_{ij}^6}{r_{ij}^6} - f_{ij}^{(8)}(r_{ij}) \frac{C_{ij}^8}{r_{ij}^8}. \qquad (20)$$

Here the first term is the repulsion term, and the last two terms describe the dispersion effects using dispersion damping functions[21]

$$f_{ij}^{(n)}(r_{ij}) = 1 - e^{-(b_{ij}^n r_{ij})} \sum_{k=0}^{n} \frac{(b_{ij}^n r_{ij})^n}{k!}. \qquad (21)$$

This MD code employs periodic boundary conditions to avoid errors that could arise at the surfaces of the MD cell. The short range interactions are assumed to be negligible for large intermolecular distances, so they are only calculated for radii under half the MD cell length. An illustration of this can be seen in Figure 8. We note that the short term interactions between two ionic species can be completely described using six parameters: B, a, C^6,C^8, b^6, and b^8.

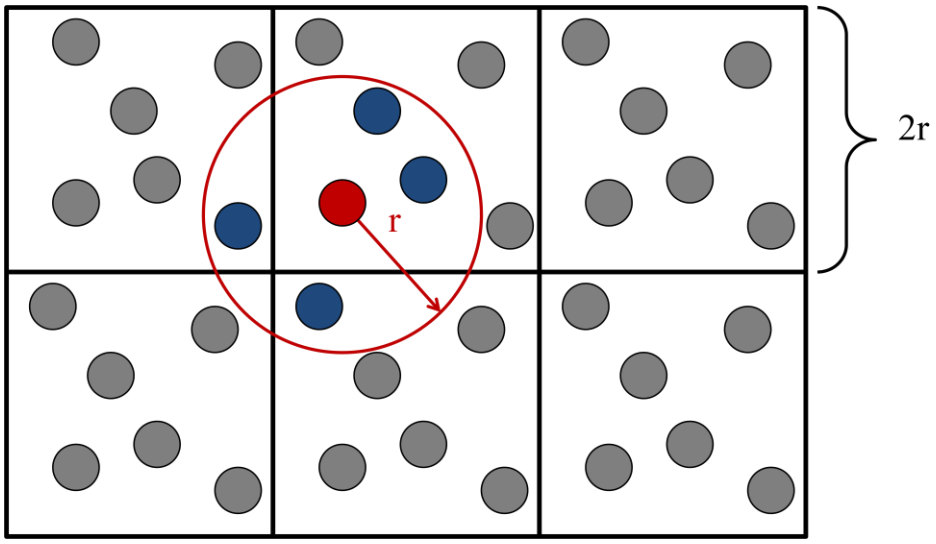

Figure 8: Periodic boundary conditions in a 2D MD cell. The cell is tessellated to form a continuum of MS. Short range interactions for an ion (red) are calculated using ions (blue) under half of a cell length away. Long range interactions take all ions into account using Ewald summation.

The long range interactions in a molten salt comprise of Coulombic interactions and ionic polarizations. A complete description of these interactions is very complex because it involves an infinite sum over the periodic boundary conditions of the MD cell. A method of calculating these interactions called Ewald summation[12] exists and is implemented in the MD code[21]. For our purposes, it suffices to say that the long range interactions between two ionic species are described by three parameters: b, c_{+-}, c_{-+}, as well as each species' polarizability, α.

The full set of interaction potential parameters used in this study is detailed in Table 1. All of these potentials with references indicated were taken from other sources that calculated the parameters directly using *ab initio* density function theory (DFT). Therefore, these values are based upon first-principle calculations of the material's electronic structure. We have estimated the values for Pu^{3+} interactions to be the same as those of La^{3+} based on studies which have

Table 1: Interaction Potential Parameters

		Short Range Interactions (a.u.)						Long Range Interactions (a.u.)				
Ion Pair	**Reference**	**a**	**B**	**C^6**	**C^8**	**b^6**	**b^8**	**b**	**c_{+-}**	**c_{-+}**	**α (1st ion)**	**α(2nd ion)**
Cl^--Cl^-	22	1.53	100	222	745	1.7	1.7	-	-	-	20	20
Cl^--Na^+	21	1.73	67.5	37.4	167	1.7	1.7	1.76	0.70	3	20	0.89
Cl^--K^+	21, 23	1.59	82.9	89.8	544	1.59	1.59	1.63	0.92	3	20	4.71
Cl^--Li^+	21, 23	1.59	15.6	1.08	4.08	1.59	1.59	1.861	0	2.08	20	0
Cl^--La^{3+}	22	1.8	450	97.2	600	1.5	1	1.258	1	1	20	10
Cl^--U^{3+}	22	1.8	400	97.2	600	1.5	1	1.258	1	1	20	10
Cl^--Pu^{3+}		1.8	450	97.2	600	1.5	1	1.258	1	1	20	10
Na^+-Na^+	21	5	1	10	100	1.7	1.7	-	-	-	0.89	0.89
Na^+-La^{3+}		5	1	12.0	54.8	1.5	1	-	-	-	0.89	10
Na^+-U^{3+}		5	1	12.0	54.8	1.5	1	-	-	-	0.89	10
Na^+-Pu^{3+}		5	1	12.0	54.8	1.5	1	-	-	-	0.89	10
La^{3+}-La^{3+}	22	3	15	47.7	100	1.5	1	-	-	-	10	10
La^{3+}-Pu^{3+}		3	15	47.7	100	1.5	1	-	-	-	10	10
U^{3+}-U^{3+}	22	3	15	47.7	100	1.5	1	-	-	-	10	10
U^{3+}-Pu^{3+}		3	15	47.7	100	1.5	1	-	-	-	10	10
Pu^{3+}-Pu^{3+}		3	15	47.7	100	1.5	1	-	-	-	10	10
K^+-K^+	23	2.65	175	32.7	151	2.64	2.64	-	-	-	4.71	4.71
K^+-Li^+		3.16	328	0.64	.004	3.16	3.16	-	-	-	4.71	0
Li^+-Li^+	23	3.68	482	0.01	0	3.68	3.68	-	-	-	0	0

shown that Pu^{3+} and La^{3+} have similar ionic radii and activity coefficients[24,25]. La is also frequently used as a Pu surrogate in experimental studies which do not have access to radioactive material, and will be used in an ADSMS test system before any highly radioactive isotopes are introduced. The Na^+-La^{3+} and Na^+-U^{3+} parameters were chosen to represent that these cations only interact via Coulombic forces. Lastly, the Li^+-K^+ short range interaction potentials were calculated by combining Li^+-Li^+ and K^+-K^+ data. This should not greatly affect our simulation results because cations are shielded from each other by large amounts of Cl^- making their interaction very weak, to the point of being almost negligible[21]. For this reason the cation-anion parameters affect our simulations much more than the cation-cation ones.

Simulation parameters and methods

As ions move in a MD simulation, the forces they experience change dynamically. This means every time the computer calculates an ion's trajectory, the ion's position can only be advanced a small amount before the trajectory has to be updated to take into account the new forces the ion experiences. For this reason MD simulations run with extremely small time steps and can only realistically simulate a system for fractions of a second. In this study, a time step of 1 fs is used when simulating an NPT ensemble. For modeling dynamic properties it proves useful to have more accurate data on each ion's trajectory. We therefore choose to update NVT ensembles twice as frequently, corresponding to a 0.5 fs time step.

The temperature of each simulation is controlled by a Nosé-Hoover thermostat algorithm. This method modifies the Hamiltonian of the system in order to simulate interaction with a heat bath[12]. This type of thermostat was chosen because it modifies the motion of each ion in a continuous way. Other thermostats, such as the Andersen thermostat, suddenly increase or decrease the energy of an ion to keep the system's temperature constant. This would make it difficult to calculate dynamic properties of the system. We alter the strength of the thermostat by specifying its relaxation time– the amount of time the thermostat takes to bring a random temperature fluctuation back to the set equilibrium value. For NPT runs we use a relaxation time of 2 ps. In order to keep the thermostat from altering our transport property data too much, a weaker thermostat having a relaxation time of 10 ps is used for NVT runs.

An Andersen barostat was used in NPT runs to hold the pressure of the system constant. Like the Nosé-Hoover thermostat this method alters the system's Hamiltonian to keep the pressure

constant[26], and has a user-supplied relaxation time. We chose to run our simulations with a relaxation time of 2 ps at a pressure of 1 atm. Use of this barostat allows the MD cell to expand or contract until a natural equilibrium is reached. This flexibility in volume is advantageous for calculating the system's density.

After initializing all parameters, each MS sample was allowed to equilibrate in an NPT ensemble for between 100,000 to 500,000 time steps. This step prevents any transient behavior caused by changing user-supplied inputs, such as the sample's temperature, from affecting the data used to calculate salt properties. The output of this run was then used as the input for a NPT data run of 500,000 time steps. Density, heat capacity, and RDFs were all calculated using this NPT data. Next the output of this run was put into a NVT data run of either 5 or 10 million time steps. This data is used to calculate the salt's transport properties. A summary of the time lengths used in each ensemble can be found in Table 2.

It should be noted that the MD code used here assumes the input is in liquid state. It is not capable of correctly modeling the dynamics that occur during a melting or freezing phase transition. Because of this, we must make sure we are modeling the molten salt in the correct temperature regime so the cell starts as and remains a liquid. If the system seems to behave like

Table 2: Simulation Parameters for Data Runs

Ensemble	**Time Step**	**Total Simulation Length**		**Thermostat**		**Barostat**	
	(fs)	(ps)	(10^3 t.s.)	(ps)	(t.s.)	(ps)	(t.s.)
NPT	1	500	500	2	2,000	2	2,000
NVT	0.5	2,500-5,000	5,000-10,000	5	10,000	-	-

a solid, it can be annealed in a high temperature NPT run for 500,000 time steps to melt it again. The temperature can then be slowly lowered to an appropriate value.

Calculating Green-Kubo functions

In order to use Green-Kubo functions to extract transport properties from our simulations, we must first calculate the appropriate correlation functions, $\langle j_a(t) \cdot j_b(0) \rangle$. This is done by first selecting an origin, t_o, within the data set (usually at the beginning), and calculating the function, $j_a(t+t_0) \cdot j_b(t_0)$, for the next few picoseconds. The origin is then moved down the data set to a new point, $t_{n+1}=t_n+t_c$. Here t_c is a constant value chosen to be larger than the correlation function's characteristic decay time, the average time for the function to decay to zero. This

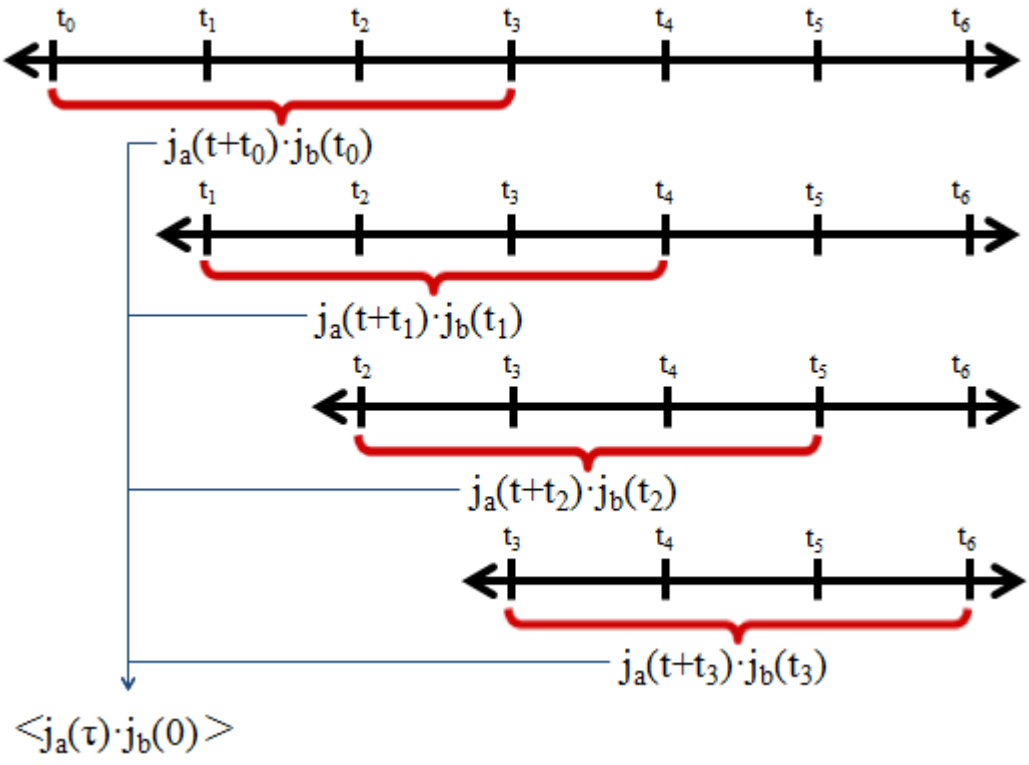

Figure 9: A diagram of the calculation of correlation functions. The correlation is found on subsets (red) having different origins, and the results are averaged (blue arrow) to give the overall correlation function.

requirement on t_c is needed to ensure that the measurements of the correlation function are not interdependent[12]. After the origin is redefined the function $j_a(t+t_1)\cdot j_b(t_1)$ is tabulated. This process of redefining the origin and calculating $j_a(t+t_n)\cdot j_b(t_n)$ is repeated for the entire data set. All $j_a(t+t_n)\cdot j_b(t_n)$ are then averaged together to give the correlation function $\langle j_a(\tau)\cdot j_b(0)\rangle$. This process, which is illustrated in Figure 9, requires a large amount of data in order to converge to a single correlation function. This explains why we chose our NVT runs to be significantly longer than their NPT counterparts.

Next, the correlation functions are integrated and multiplied by appropriate constants to yield the Green-Kubo function of interest. These functions eventually reach a plateau value at a time corresponding to when the correlation function decays to zero. This plateau is averaged over for 1ps to yield the final value of the transport property of interest. Examples of correlation functions and their corresponding Green-Kubo functions are shown in Figure 10. All correlation

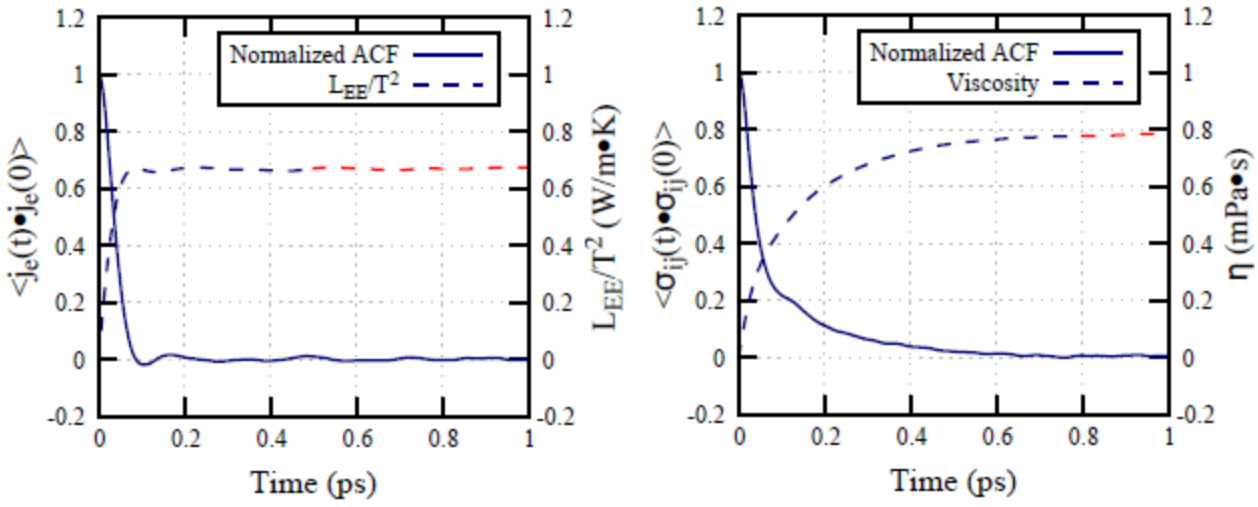

Figure 10: Autocorrelation and Green-Kubo functions for NaCl at 1300K. Both ACFs have been normalized for comparison. The functions used for calculating the largest term for λ (left) converge much more quickly than the viscosity functions (right). The plateau region is shown in red.

functions used for calculating λ and σ converged quickly, within 200fs. We therefore chose t_c= 200 fs and calculated each Green-Kubo function for 2 ps. The plateaus were averaged from 1 to 2 ps. The correlation functions used in viscosity calculations converge much more slowly, with t_c varying from 500 to 5000 fs. We therefore chose t_c on a case by case basis and averaged over the Green-Kubo plateau for 1 ps after the correlation function converged.

Error calculations

It is important to establish error estimates so that any discrepancies between our estimated values and physical quantities can be accounted for when engineering an ADSMS system. We divide the error of our simulations into two parts: statistical error and modeling error. Statistical errors originate from the data set size and random thermal fluctuations in the simulated system. The statistical error is determined by splitting the data set up into 30 to 50 smaller blocks and running transport property calculations on these smaller chunks. The average and variance of this

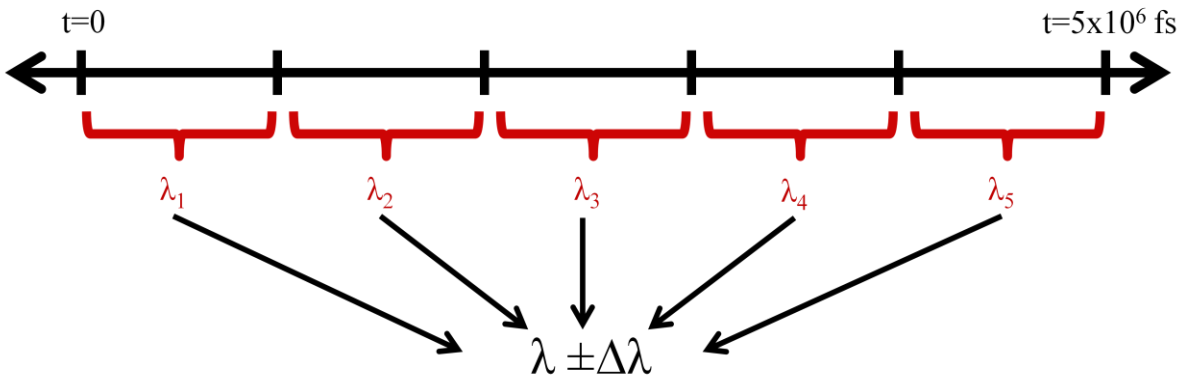

Figure 11: A diagram of the statistical error calculation. The data is parsed into between 30 and 50 smaller subsets (5 shown here) and the calculation is run multiple times. The results are then averaged together to give a final estimate and error.

smaller data set then gives an estimate and error for the transport property in question. A schematic of this process is shown in Figure 11. Modeling error accounts for all other simulation errors due to the MD code, interaction potential parameters, and thermostat and barostat effects. There is no explicit way of calculating this error, but we estimate it to be approximately 5% after comparing our simulations with experimental data.

Density and heat capacity measurements do not involve Green-Kubo relations, and therefore have very low statistical errors, on the order of 0.1%. We therefore only consider modeling errors for these properties. On the other hand, transport properties have statistical errors of 10% or more, even though ten times more data must be collected in order to calculate them. This is because the averaging operation $\langle j \cdot j \rangle$ in equations (17) - (19) only converges when calculated over a very large data set. In this situation, we make an estimate of the total error based on the relative values of the statistical and modeling error.

Hardware

The simulations done in this study used the Texas A&M Accelerator Research Lab's high performance computing cluster. This cluster contains a head node containing 2 8-core CPUs and 16Gb of memory, as well as 8 Dell Power Edge R815 computational nodes each having 4 12-core processors. Each computational node has access to 128 Gb of memory and is connected to the head node by both a private Ethernet LAN and a 40 Gbit/s Infiniband switch. The system runs Scientific Linux 6.0. This study used an estimated 30,000 CPU hours and produced approximately 3Tb of usable raw data.

CHAPTER IV

BINARY SYSTEMS

We begin by examining binary MSs, only having a single anion and cation. The wealth of data on pure salt systems makes this a natural starting place to verify our modeling methods. X-ray and neutron diffraction studies probe the microscopic structure of the melt, and the subsequent data provides an avenue to validate our interaction potential parameters by comparing simulated RDF's with experimental results. Furthermore, it has been shown in mixed chloride systems that the positions of the first cation-anion RDF peak are almost identical to the peak positions in the corresponding pure salt[27]. Thus, if all the first RDF peaks match experiment for the pure constituents of a fuel mixture, the first peak positions of the fuel should also be correct. After checking the RDFs, we calculate the other properties of these salts and compare them with experimental information in order to extensively affirm our methods. Here we look to two different types of binary system: alkali chlorides and heavy metal chlorides.

Alkali chlorides (LiCl, NaCl, KCl)

Three alkali chlorides are of interest to us. The most important is sodium chloride; almost 70% of our fuel salt will be comprised of NaCl making adequate modeling of this compound an essential first step in understanding the properties of the entire fuel salt. LiCl and KCl comprise the secondary coolant salt. The study of these additional salt systems allow us to make a more robust and thorough evaluation of the model.

These simulations were carried out in a system of 512 ions. The simulation cells were built as crystalline solids. Each of these binary systems have well known crystal strctures. When a cell is created, the code calls an input file mapping the location of the ions to this solid crystal structure. To simulate melting, the solid system is annealed at high temperature or given a "kick" of energy. To run our computational experiments, the cell is then cooled to the temperatures of interest. LiCl has a lower freezing point (883K) than NaCl (1073K) and KCl (1043K) [28]; its data was collected at slightly lower temperatures.

RDFs

Radial distribution functions (RDFs) were calculated for three alkali chlorides at 1300K in the NPT ensemble. Figure 12 shows the three partial RDFs for each system, which examine the relative positions of ion species *i* to that of ions of species *j*. The NaCl data is compared to experimental neutron diffraction data taken by Edwards *et al.*[29] A full set of partial RDFs for KCl and LiCl has not been reported, but the RDFs of a mixture of the two will be examined later, with the expectation that first peak position is in a similar position because it is essentially invariant when mixing pure salts.[27].

Our NaCl simulations are in good agreement with experimental values. We have correctly reproduced the first and second peak positions, except for the first peak in the Na^+-Na^+ partial RDF. However, this peak is subject to the most experimental error, and shouldn't impact our modeling due to of the lack of cation-cation interaction. It should be noted that the experimental amplitude for the Na^+-Cl^- function is slightly lower, while it is slightly higher for Cl^-- Cl^-. This discrepancy is noted by Edwards [29], and we believe could be the result of a difference in

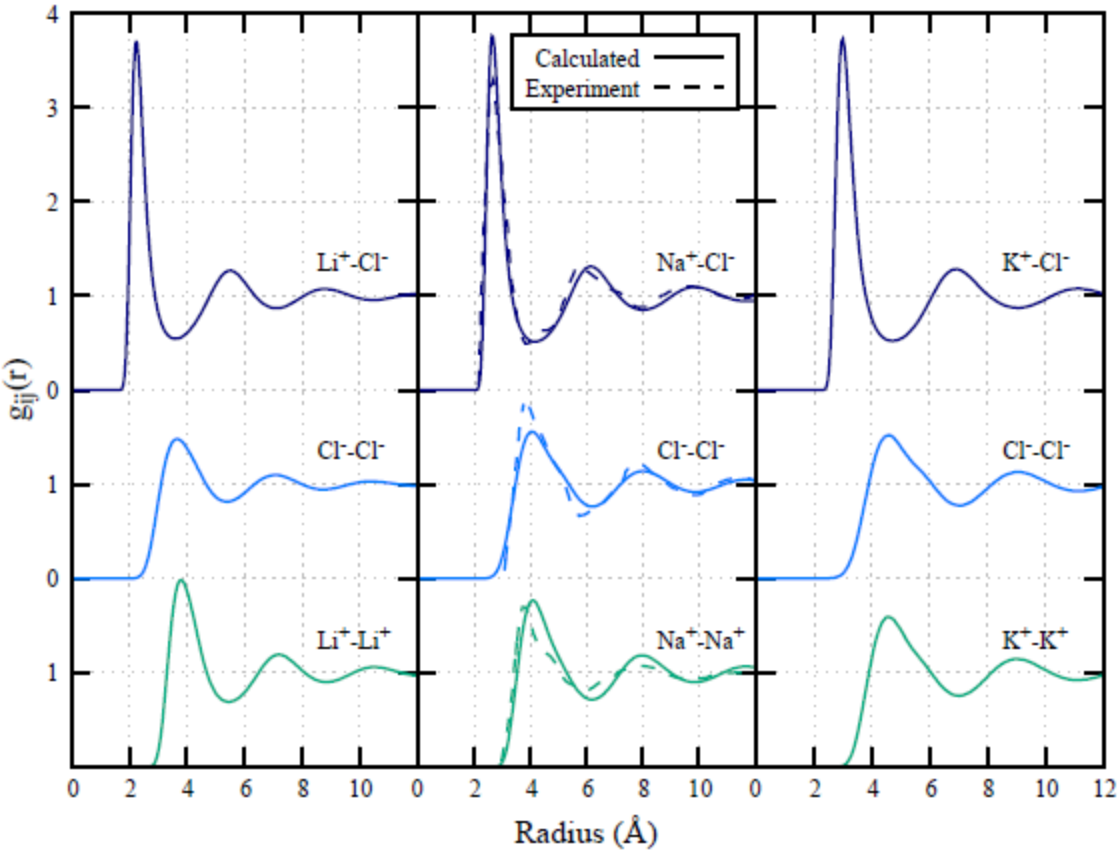

Figure 12: Partial RDFs of alkali chlorides. Each RDF is offset by 2 from the one below it. Experimental data is reproduced from Edwards *et al.*[29] As cation size increases, the first and second peak positions shift to the right.

temperature between the simulation (1300K) and experiment (1150K). Our data also exhibits a rightward shift in the first and second peaks as we move left to right across the plot. This is due to the ionic radius also increasing as temperature increases, causing the gap between ions to grow. Finally, we draw attention to the flattening of the peaks in the cation-cation RDF as ionic mass increases. This flattening effect is due to the ion polarizabilities increasing from 0 (Li) to 4.71 (K).

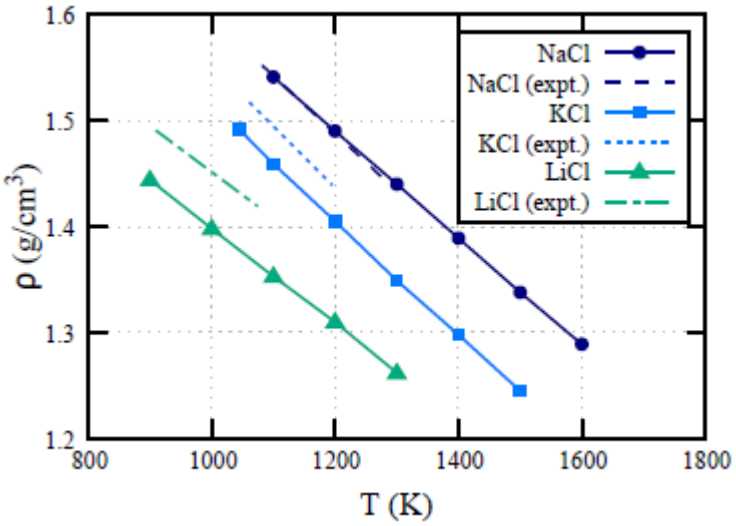

Figure 13: Temperature dependence of alkali chloride density. All three salts exhibit similar temperature dependence. Experimental data taken from Janz *et al.*[28]

Density and heat capacity

The densities of all three alkali chlorides are shown in Figure 13. We obtain excellent agreement with experiment here, with deviations in ρ of less than 5%, 3%, and 1% for LiCl, KCl, and NaCl respectively. In order to evaluate the temperature dependence of these systems, a line having the form $\rho(T)=\beta_d-\alpha_d T$ was fit to each of the data sets. Our simulations predict α_d to within 8% for KCl, 7% for NaCl, and 3% for LiCl. It is a nice coincidence that NaCl is the densest alkali chloride, due to its mass to ionic radius ratio. This means a fuel salt based on NaCl instead of KCl or LiCl will have a larger mass density which benefits the spallation process. Finally, we note that all these chlorides do in fact have the positive coefficient of thermal expansion which is desired for the ADSMS system because it leads to negative thermal reactivity feedback [7].

The heat capacities of these systems are reported in Figure 14. They are given by the slope of the enthalpy vs. temperature data collected during NPT simulations. All three systems have

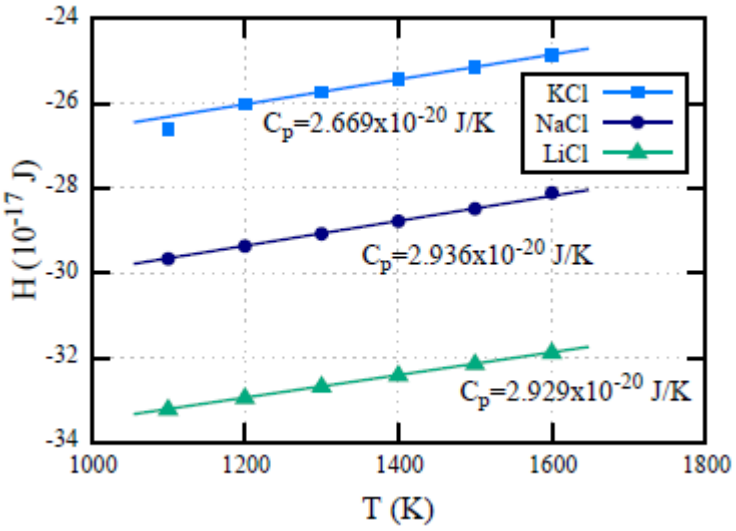

Figure 14: Enthalpy vs. temperature for alkali chloride systems. The heat capacity is given by the slope of the line of best fit. All three salts have very similar heat capacities, but their specific heat capacities vary greatly.

similar heat capacities, which is likely due to their similar microscopic structures. This also means that their specific heat capacities, obtained by dividing C_p by the simulation cell mass, are quite varied. Our results agree quite well with experiment; KCl's c_p has under 7% error, while both NaCl's and LiCl's are within 3% [30]. The calculated and experimental specific heat capacities are summarized along with the density parameters in Table 3. We have achieved less than 8% deviation from experiment, and shown the similarity in the temperature dependence for three different alkali chloride systems.

Table 3: Summary of Alkali Chloride NPT Data

Salt	**α_d (10^{-4} g/cm^3•K)**		**β_d (g/cm^3)**		**c_p (kJ/K•kg)**	
	This Work	**Experiment[28]**	**This work**	**Experiment[28]**	**This work**	**Experiment[30]**
LiCl	4.48	4.38	1.84	1.88	1.48	1.44
NaCl	5.06	5.43	2.10	2.14	1.18	1.15
KCl	5.39	5.83	2.05	2.14	0.92	0.98

Transport Properties

The thermal conductivity, electrical conductivity, and viscosity were calculated using a NVT run of 5 million time steps. λ is plotted against temperature in Figure 15, along with experimental data from Nagasaka *et al.*[31] The functions extrapolated from the simulation data have the form $\lambda(T)=\beta_t-\alpha_t T$. There is almost no deviation from experiment for the KCl cell; although, the temperature dependence is exaggerated in this model. For the NaCl sample, both the temperature dependence and the actual λ are overestimated. This could be an experimental artifact: the experimental data was taken by measuring system's thermal *diffusivity* and then multiplying by ρ and c_p to yield λ. Thus, errors of less than 8% from the previous NPT simulations might contribute to some of this discrepancy. Additionally, the experimental data has a quoted uncertainty of 8%. Finally, we remark that Ohtori *et al.* encountered a similar overestimation effect when simulating alkali chlorides[32], calculating values for NaCl and LiCl that are similar to the ones presented here. The extremely large statistical errors present in the

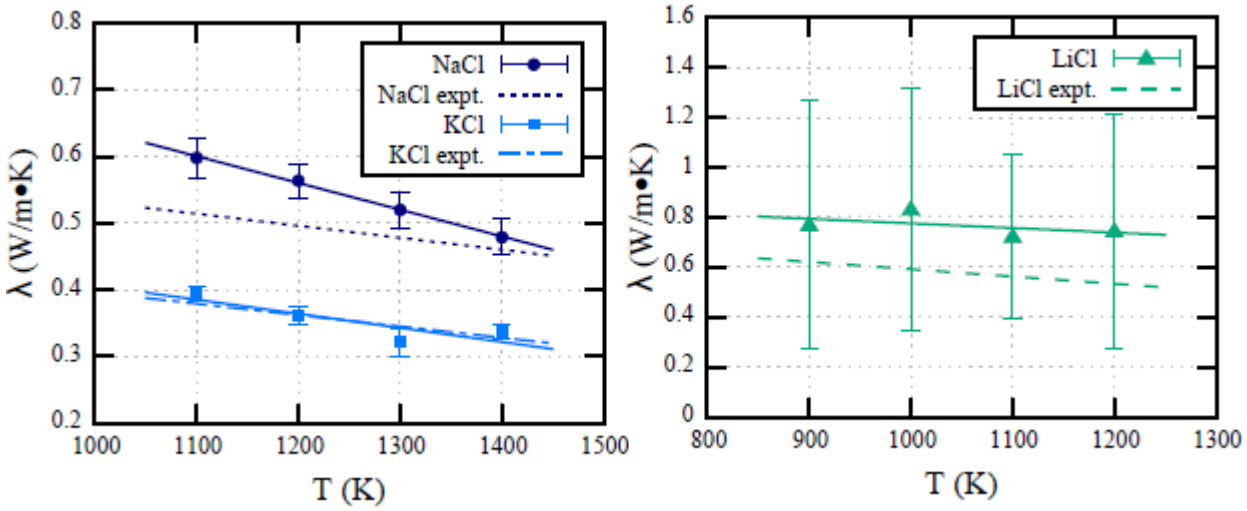

Figure 15: Thermal conductivity of alkali chlorides. Error bars shown only take statistical error into account. The experimental data is reproduced from thermal diffusivity measurements by Nagasaka *et al.* [31]

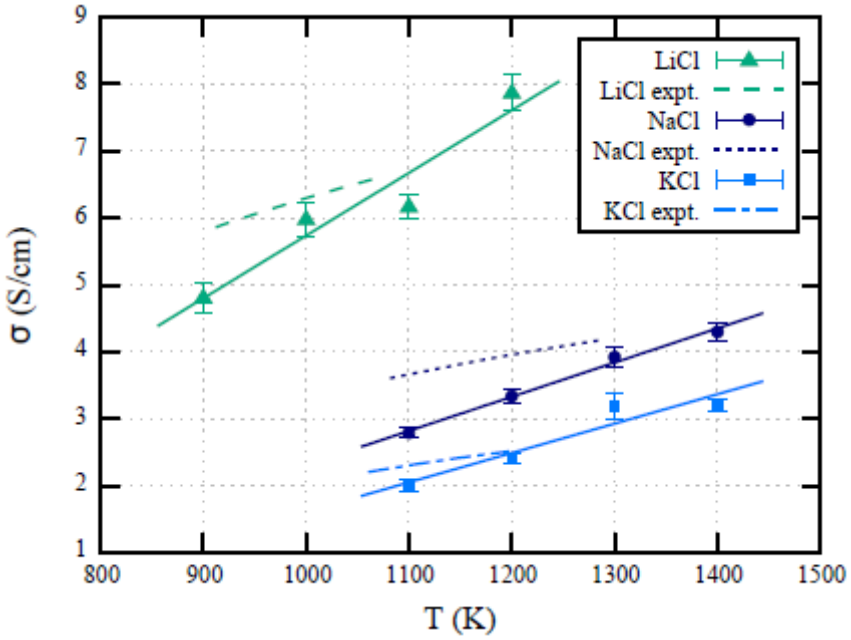

Figure 16: Electrical conductivity of alkali chlorides. Experimental data having Arrhenius form is taken from Redkin *et al.* [33] Our results underestimate σ at lower temperatures, but overestimate it the temperature dependence.

LiCl data have been encountered and discussed before by Ohtori *et al.*[21] They are an artifact of two very large terms being subtracted from each other in the λ calculation. This causes the terms to have errors of a size similar to that of the difference between these terms, increasing the relative error. This effect is inherently a result of the large mass difference between the anions and cations in the LiCl melt.[21]

Figure 16 displays the simulation results for σ, plotted with experimental data[33]. Our results are modeled as having an Arrhenius temperature dependence of form $\sigma(T)=\sigma_0 \exp\left(\frac{E_1}{RT}\right)$ in order to facilitate comparison with experiment. The two constants were determined by performing a linear fit of the line having form $\ln \sigma = \frac{E_1}{RT} + \ln \sigma_0$. However, the data behaves very linearly,

causing it to be notably lower than experimental data near each salt's freezing point, but this gap is closed after the salt is heated by a few hundred K. This temperature profile is probably caused by the code's inability to simulate conductivity due to electron flow; it only considers charge propagation due to bulk ionic flow. As the temperature decreases, the ratio of ionic flow to electron flow decreases, causing the code to underestimate the electrical conductivity by an increasing amount. The bulk ionic flow does have enough of an impact to allow an estimation of σ. Our calculation's maximum deviation from experiment, 31%, occurs just under 1100K for NaCl and decreases with temperature. According to this data we expect our simulations to underestimate σ when the temperature is close to the salt's freezing point.

Lastly, we show the results of the viscosity calculations in Figure 17. The solid curves in the

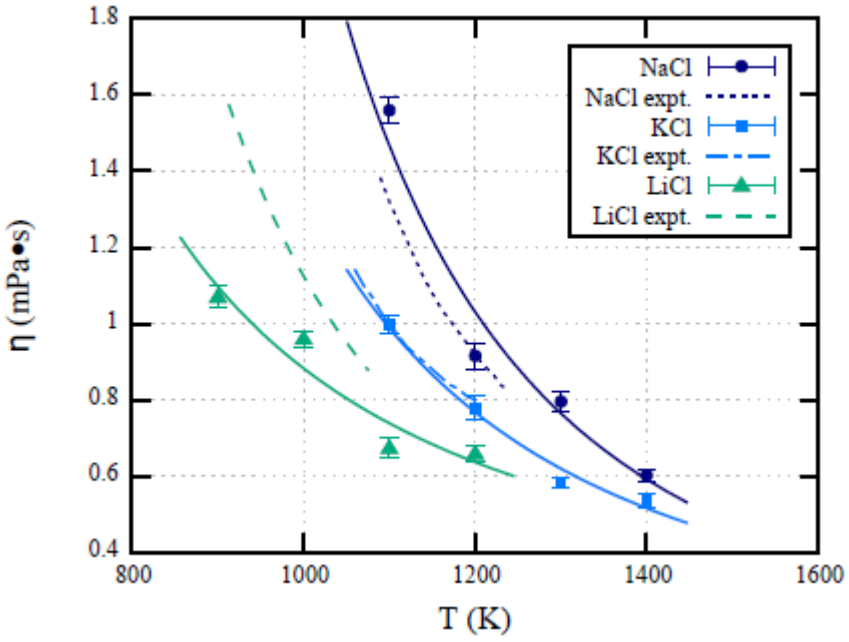

Figure 17: Shear viscosity of alkali chlorides. Experimental data taken from Janz *et al.*[28] The best fit lines have Arrhenius form.

Table 4: Fit Parameters for Alkali Chloride Transport Properties

Salt	Sources	λ (W/m·K)		σ (S cm^{-1})		η (mPa·s)	
		α_t (x10^{-4} W/m·K^2)	β_t (W/m·K)	σ_0 (S cm^{-1})	E_1 (J mol^{-1})	η_0 (mPa·s)	E_2 (J mol^{-1})
LiCl	This work	1.839	0.960	29.04	-13,441	0.1249	16,261
LiCl	28,31,33	2.900	0.882	13.13	-6,098	0.0331	29,317
NaCl	This work	4.010	1.042	21.91	-18,787	0.0214	38,681
NaCl	28,31,33	1.800	0.712	7.64	-6,743	0.0185	38,957
KCl	This work	2.115	0.618	22.25	-21,924	0.0478	27,695
KCl	28,31,33	1.700	0.566	6.95	-10,100	0.0531	26,891

plot have Arrhenius form, with constants $\eta_0$and E_2. These results mirror our λ findings; there is almost perfect agreement with experiment for KCl and good agreement for NaCl. The results for LiCl are underestimated temperatures near the freezing point, but seem to converge towards experimental value with increasing temperature. These results are quite successful when it is considered that the material's viscosity is generally the most difficult property to have converge properly. We remark that all three of these viscosities are in the same regime as that of water at 300K. Thus, water can serve as a first order approximation when determining types of pumps and pipes used for transporting these types of salts.

We have summarized our results as well as the plotted experimental data for the transport properties of alkali chlorides in Table 4. Although our simulations are not perfect, we achieved excellent agreement with the properties of KCl. The maximum of discrepancy for any transport property in the NaCl system is 30%, a value which quickly diminished with increasing temperature. Furthermore, this value was calculated for electrical conductivity, which is of least importance when designing the ADSMS system. Finally, the LiCl simulations have yielded

good first order estimates, but have large statistical errors due to the difference in cation and anion mass and the proximity of the simulation temperatures to its freezing point.

Trichlorides ($LaCl_3$, UCl_3)

Before considering the addition of transuranics to our simulations, we turn to two trichlorides of interest, UCl_3 and $LaCl_3$. The larger ratio of anions to cations changes the structure of the melt, as each cation is surrounded by more negatively charge ions. We chose to examine UCl_3 because its interaction potential parameters are very similar to those of $PuCl_3$, which is to be used in the fuel salt. Furthermore, it will help us describe any issues associated with a large mass discrepancy between heavy transuranics and chlorine (since U^{3+} has a mass which is almost 7 times that of Cl^-). $LaCl_3$ is also examined because there is much more experimental data available for $LaCl_3$ than either UCl_3 or $PuCl_3$. Additionally, it is commonly used as a Pu surrogate, allowing us to the same interaction potentials for La and Pu.

These simulations were performed with cells containing 90 cations and 270 anions. The cells were built from existing MD simulations by strategically deleting or changing cation species. After this process, the cells were annealed and equilibrated. The mass of the U used in these simulations was 238.02 u.

RDFs

RDF data was gathered at 1200K for $LaCl_3$ and at 1300K for UCl_3. Figure 18 compares the total RDF of $LaCl_3$ to X-ray diffraction data collected by Okamoto *et al.*[34] Both values are offset from the calculated partial Cl^--Cl^- RDF. At first glance, our function seems to be incorrect,

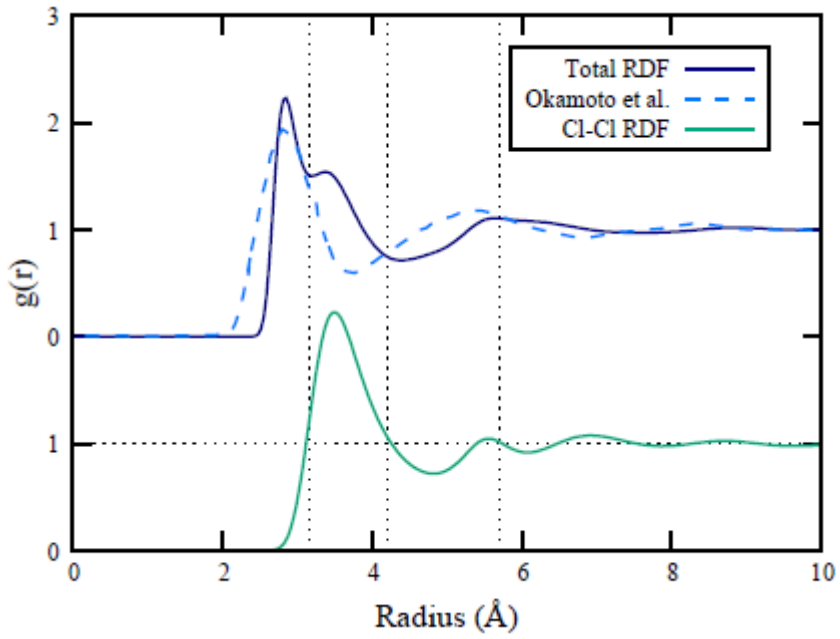

Figure 18: Total RDF of $LaCl_3$ compared to experiment. Our simulated RDF contains and extra peak, which can be explained by the Cl^--Cl^- interaction, which is offset below. The experimental data is reproduced from the X-ray diffraction work of Okamoto *et al.*[34]

having an extra peak just behind the first, followed by a large valley. However, Okamoto notes that the X-ray diffraction technique does not probe the Cl^--Cl^- interaction. We would therefore expect our calculated RDF to contain some extra structure due to these interactions. Comparison with the partial Cl^--Cl^- RDF shows that this is the case; intervals where the partial RDF exceeds or is less than unity directly correlate to areas where our total RDF over predicts or underestimates the experimental RDF. This weighting of experimental RDFs based on how well they probe certain interactions is also discussed by Okamoto in his work with UCl_3[35]. We also note that the first peak in the experimental data is shorter and broader, but we believe this is due to the inclusion of a damping factor in the experimental data, which widens the RDF[35].

Our study of the UCl_3 partial RDFs is shown in Figure 19 where they are compared to partial RDFs simulated by Okamoto[35]. We have nearly perfect agreement, which is to be expected because the short range simulation potential parameters used in both studies were identical. Our study does, however, use a slightly different method for handling the long range interactions. The partial RDFs illustrated were also shown by Okamoto to be consistent with X-ray diffraction experiments once the damping factor and interaction weighting are taken into account.

Comparison of these RDFs with those of alkali chlorides reveals the difference in structure for

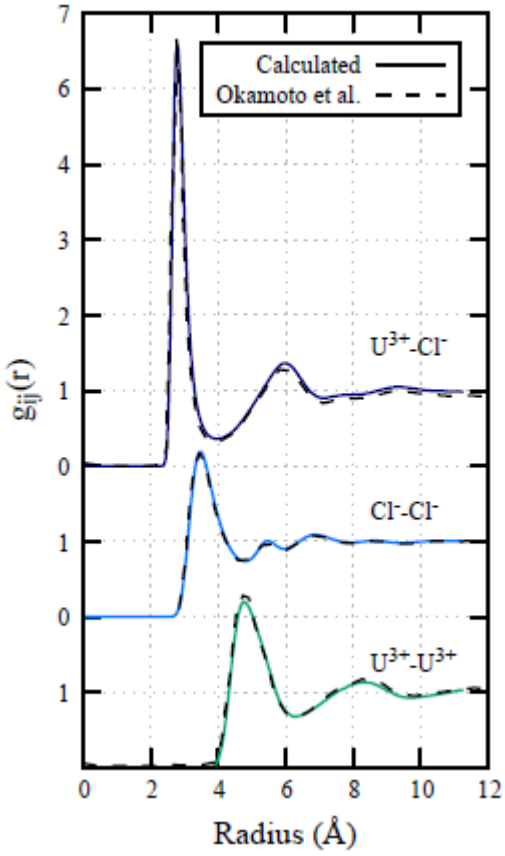

Figure 19: Partial RDFs of UCl_3. We get excellent agreement with previous work by Okamoto *et al.*[35] These RDFs agree well with X-ray diffraction data. Each RDF has a vertical offset of 2 from the one below it.

trichlorides. The first peak for the cation-anion functions are much higher than those of the alkali chlorides, corresponding to more chlorides being directly adjacent to the cations. Furthermore, both the trichloride cation-cation and anion-anion RDFs have a much narrower first peak, with the anion-anion peak occurring before the cation-cation one. This indicates that the cation is surrounded much more by anions. This once again agrees with measured values, as the coordination number - the number of anions surrounding a cation - for molten NaCl is about 6[29], while it is 8 for UCl_3[35].

Density and heat capacity

The densities of the two studied trichlorides are graphed against temperature in Figure 20. The experimental data for UCl_3 was collected by Desyatnik *et al.*[36], while the data for LaCl3 is

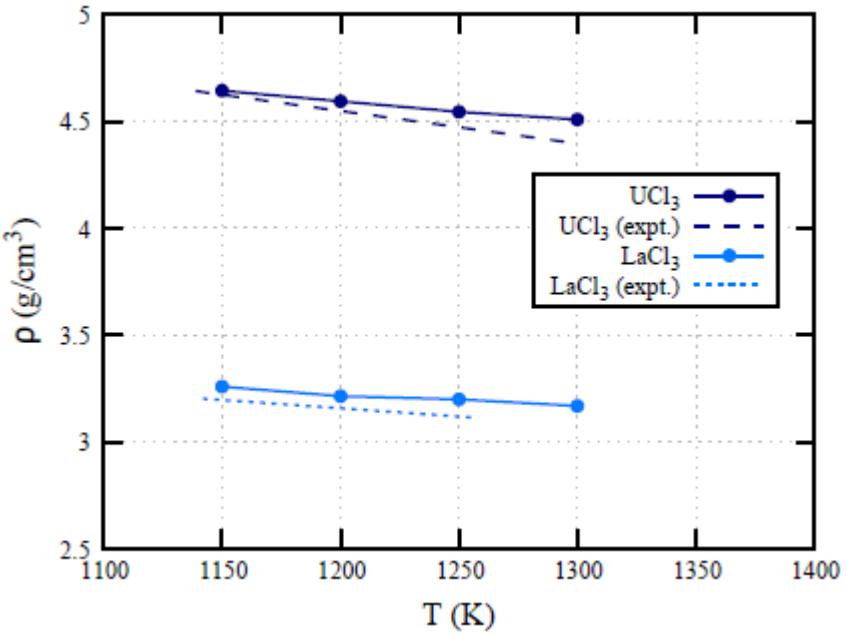

Figure 20: Simulated densities for chosen trichlorides. Our simulated data is very close to the experimental data for UCl_3[36] and $LaCl_3$[28]. Despite having a different cation to anion ratio, the temperature dependence is close to that of the alkali chlorides.

reported by Janz *et al.*[28] We have achieved accurate results, with deviations from experiment of less than 3% in both systems. We comment that our results seem to slightly underestimate the strength of the temperature dependence, but note that the values of α_d are of the same order of magnitude has those calculated for the alkali chlorides. The difference in densities between UCl_3 and $LaCl_3$ can be attributed entirely to the mass of the cations; the U and La ions interact with Cl in essentially the same way, but the U is 1.8 times as heavy. UCl_3 also has larger temperature dependence because the inverse volumes of both salts vary in a similar fashion, but this variation is amplified when it is multiplied by a larger mass during the density calculation. We can expect similar behavior for $PuCl_3$ because we are using the La interaction potentials, but the mass of Pu is only slightly larger than that of U.

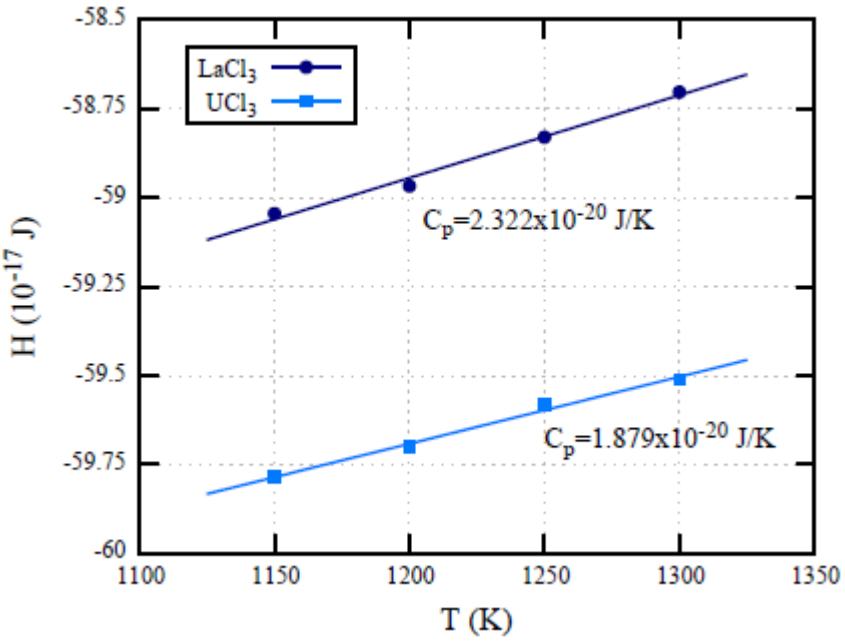

Figure 21: Enthalpies and the heat capacity for trichloride salts. The heat capacity of UCl_3 is 20% less than that of $LaCl_3$. These values cannot be compared to the calculations for alkali chlorides, because of the different number of ions used

Table 5: Summary of Trichloride NPT Data

Salt	α_d (10^{-4} g/cm^3•K)		β_d (g/cm^3)		c_p (kJ/K•kg)	
	This Work	**Experiment**	**This work**	**Experiment**	**This work**	**Experiment**
$LaCl_3$	5.701	7.774 [28]	3.908	4.090 [28]	0.633	0.645 [37]
UCl_3	9.079	15.222 [36]	5.684	6.375 [36]	0.365	-

Examination of the trichloride heat capacities, shown in Figure 21, reveals that the heat capacity of UCl_3 is about 20% less than that of $LaCl_3$. This indicates that the larger cation size may increase the thermal response to changes in system energy. The values for heat capacity cannot be strictly compared to those calculated for the alkali chlorides, because the simulations used a different number of ions, but they are in the same neighborhood of values. The specific heats can be compared, however, and are much smaller for the trichlorides. This is undoubtedly due to the much larger amount of mass in the trichloride cations. We were unable to find experimental data on the specific heat capacity of UCl_3, but our $LaCl_3$ results are within 2% of the data taken by Dworkin and Bredig[37]. On the whole our NPT simulations are able to accurately model trichloride systems, and are summarized in Table 5.

Transport properties

We performed NVT simulations of 5 million time steps for $LaCl_3$ and 10 million time steps for UCl_3. The extra time for the UCl_3 runs was required to achieve proper convergence of the viscosity ACFs at lower temperatures, where they had characteristic time lengths of up to 5 ps. We have chosen not to examine λ and σ for UCl_3 because of a lack of experimental data to compare. Although we were unable to find data on the value of λ for $LaCl_3$, σ values are reported in the Janz database[28].

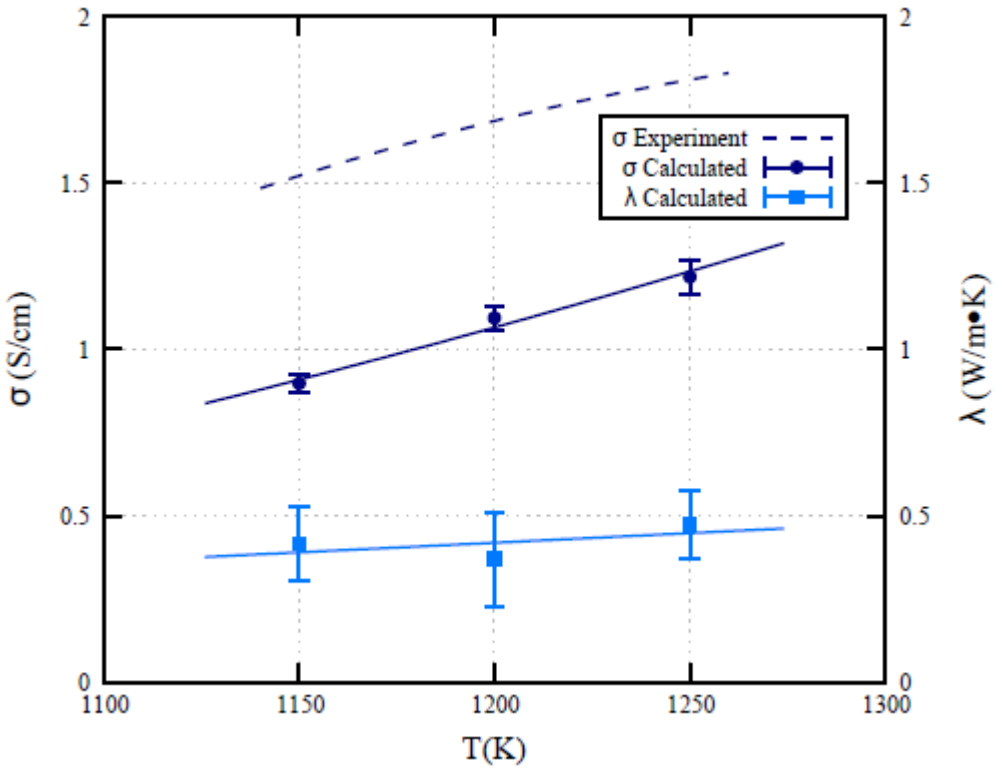

Figure 22: λ and σ of $LaCl_3$ just above the melting point. The same trend of σ underestimation exists in this system. There is a positive temperature dependence of λ, but the statistical errors are quite large. Experimental data was taken from Janz[28].

Results of our calculations for $LaCl_3$ can be seen in Figure 22. The same major trends noted in the analysis of the alkali chlorides apply to σ here; the data behaves linearly and underestimates the experimental data because of the proximity of the simulation to $LaCl_3$'s freezing point of 1143K[28]. The magnitude of this underestimation is similar to the 0.5 W/(m·K) difference seen in the alkali chloride (KCl) having the closest σ value. We are unable to compare λ to any experiment, but its value lies in the same range as the other chlorides studied. Our results have a positive temperature dependence, but it is weak when compared to the very large statistical errors, on the order of 25%, associated with this calculation. Furthermore, only three points of data were gathered for this plot, so more information is most likely needed to get an accurate

temperature dependence. Our data supports an estimation of λ=0.42±0.12 in the temperature range of 1150 to 1250K.

The viscosity was calculated for both systems and is compared to various experiments in Figure 23. We were able to find only one experiment to compare our UCl_3 data, that of Desyatnik[36]. According to this data our results significantly overestimate both the viscosity and the temperature dependence of the melt, although the discrepancy diminishes at higher temperatures. Our interaction potential may be causing the formation of multi-ion complexes with would increase the viscosity of the melt as ions try to act as part of a larger unit. This would explain

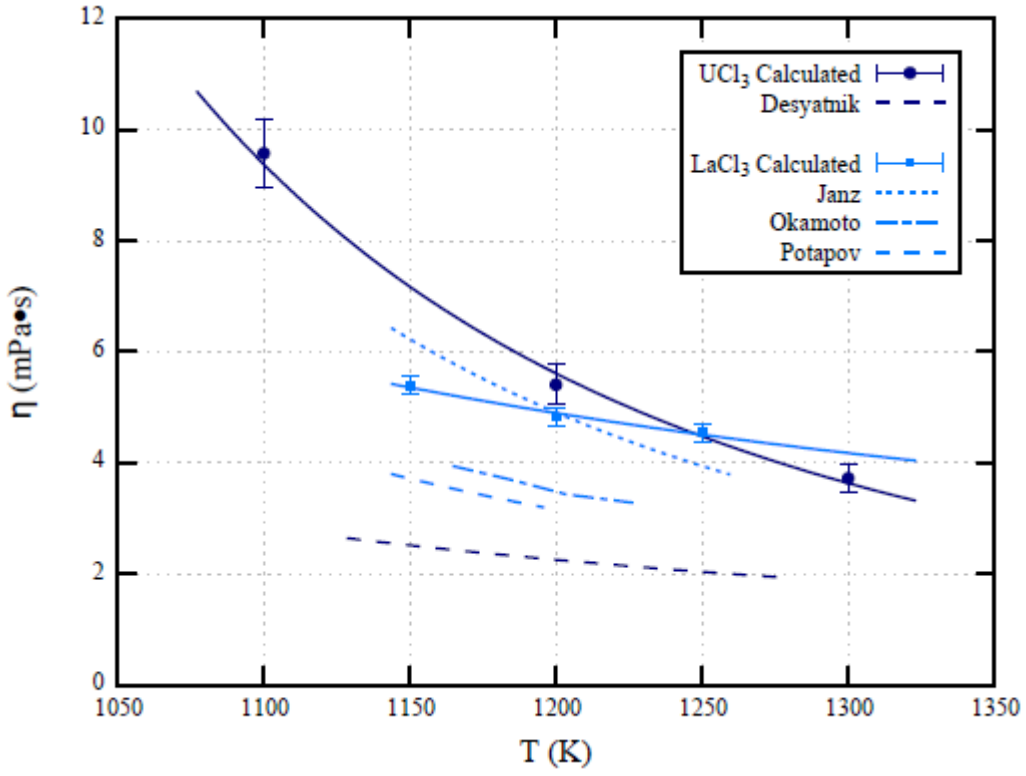

Figure 23: Viscosity of trichloride melts. UCl_3 (dark blue) overestimates the viscosity reported by Desyatnik[36]. Our $LaCl_3$ data (light blue) is within the vicinity of the data from three experiments.

large discrepancy at low temperature, as the ions with lower kinetic energy would tend to stay part of their local ion complex. These medium ranged effects are known to strongly increase viscosity and decrease σ[34]. There is ample experimental data for molten $LaCl_3$, but it varies widely since viscosity measurements of molten salts are very difficult. Our results are in the vicinity of those tabulated by Janz[28], but have temperature dependence similar to the results in Okamoto[34] and Potapov[38]. The most recent work by Potapov notes that the Janz data is probably overestimated due to oxide buildup during their salt preparation. We therefore believe these results also over predict the actual viscosity by 40% at the melting point. This discrepancy then decreases slightly with increasing temperature. Our results are within the general vicinity of all three experiments for the simulated temperature range, and we believe would be adequate as a first estimation. Finally we note that the viscosities of the trichlorides are much larger than those of alkali chlorides, due to the formation of ionic complexes, as well as a larger coordination number and cation size causing a reduced cation mobility. Furthermore, all of the trichloride melts remain very thin, having a viscosity under 10 mPa·s, which is less than most common oils. The results of the trichloride NVT simulations are summarized in Table 6.

Table 6: Fit Parameters for Trichloride Transport Properties

Salt	**Source**	**λ (W/m·K)**		**σ (S cm^{-1})**		**η (mPa·s)**	
		α_t (x10^{-4} W/m·K^2)	**β_t (W/m·K)**	**σ_0 (S cm^{-1})**	**E_1 (J mol^{-1})**	**η_0 (mPa·s)**	**E_2 (J mol^{-1})**
$LaCl_3$	This work	-5.78	-0.275	41.67	-36,577	0.6196	20,622
$LaCl_3$	28	-	-	13.52	-20,840	0.0206	54,599
$LaCl_3$	34	-	-	-	-	0.0870	36,889
$LaCl_3$	38	-	-	-	-	0.0739	37,455
UCl_3	This work	-	-	-	-	0.0198	56,334
UCl_3	36	-	-	-	-	0.1825	25,079

CHAPTER V

MULTI-COMPONENT MIXTURES

We now examine the effects of mixing two different MSs having the same anion. This is of particular interest to the ADSMS project, as all salts proposed for use in the system are multi-component mixtures. For this section, we adopt a notation where the salt name is followed by each salt's respective mole concentration in parenthesis. We first inspect the secondary salt used for cooling the ADSMS system, a eutectic mixture of LiCl-KCl (59.5,40.5%). Next, we examine the effects of altering the alkali chloride to trichloride ratio in a NaCl-UCl_3 (X, 100-X%) mixture. This will allow us to compare our results for a alkali chloride - trichloride mixture to experiment in preparation for the final step of this study. This step models the ADSMS fuel salt itself as a NaCl-$PuCl_3$-$LaCl_3$ (68,28,4%) mixture, and produces working estimates to be used while planning specific parameters of the ADSMS system.

Secondary salt (LiCl-KCl eutectic)

A LiCl-KCl mixture has been selected as the ADSMS secondary salt to absorb heat from the fuel salt in the primary heat exchanger. This mixture will be used at the eutectic concentration of 59.5% LiCl and 40.5% KCl, corresponding to where the mixture has the lowest freezing point (628K)[39]. The lower melt point allows the heat exchanger to operate at lower temperatures, increasing its performance, while preventing the solidification of the coolant. Additionally, operating at the eutectic concentration prevents phase separation caused by either LiCl or KCl precipitating out of the mixture. This mixture is also relatively inexpensive and has some of the

highest figures of merit when compared to other potential chloride coolants[39]. There are fluoride-based coolants which have better figures of merit, but fluorides tend to be more corrosive and have higher operating temperatures. The LiCl-KCl eutectic mixture is relatively well studied, but there is a curious scarcity of data on λ despite the salt's potential use as a reactor coolant.

The simulations performed here used 256 Cl^-, 151 Li^+, and 105 K^+ ions. The simulation cell was created from an existing KCl cell, by replacing 151 K^+ ions with Li^+. The system was then annealed and allowed to equilibrate. We are specifically interested in the properties around 800K, the currently planned secondary salt operating temperature.

RDFs

We take this opportunity to examine the validity of our interaction potential parameters for lithium and potassium, since we were unable to find any experimental data on these ions in pure melts. Figure 24 shows the simulated partial RDFs calculated at 700K, plotted against X-ray diffraction data taken by Okada *et al.* at 668K[27]. We have achieved excellent agreement in both peak position and height for the three partial RDF's (Li^+-Cl^-, K^+-Cl^-, Cl^--Cl^-) for which the authors were able to accurately deduce peak positions. There is also passable agreement in peak positions for the K^+-K^+ and Li^+-K^+ interactions, although slight discrepancies exist in the peak heights. The experiment was completely unable to detect the Li^+-Li^+ interaction. We note that the bottom three RDFs all involve cation-cation interactions, which are much weaker than their cation-anion counterparts. Our interaction potential parameters have therefore excellently reproduced the microscopic structure of this multi-component melt.

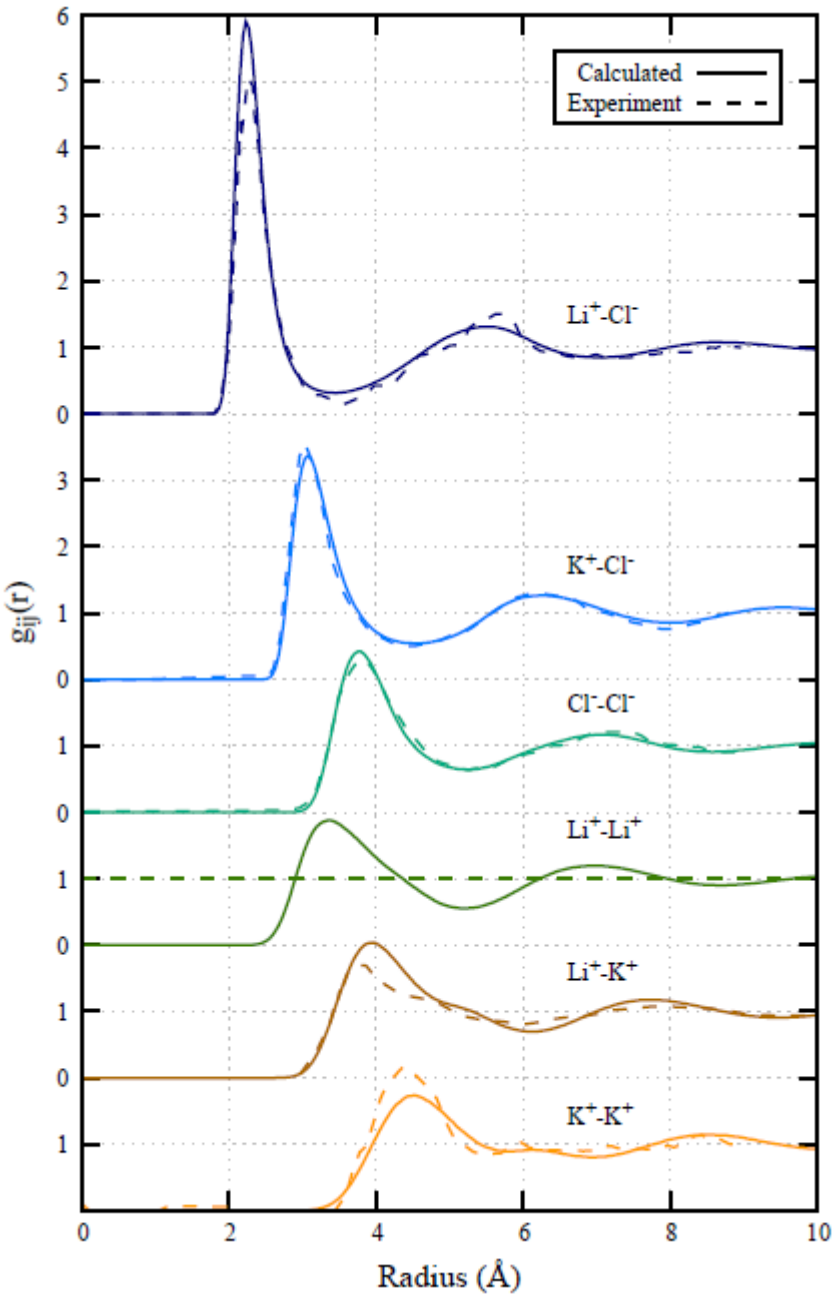

Figure 24: Partial RDFs for LiCl-KCl eutectic mixture. Excellent agreement has been achieved with the first cation-anion and anion-anion peaks found in X-ray diffraction experiments performed by Okada *et al.* [27] Vertical offsets have been added to each RDF for clarity.

As predicted, the first peak positions in this melt are likened to those calculated for pure KCl and LiCl. The heights are depressed because the ratio of each cation species to chlorine is lower in the mixture. This further supports our use of these interaction parameters in the previously performed alkali chloride simulations.

Density and heat capacity

Modeling of the density of this mixture is nearly perfect, with a maximum error of less than 1% when compared with the experimental data. This is surprising; our simulations for both LiCl and KCl predicted densities slightly lower than experiment. This hints that mixing the two salts could have caused an upward shift towards experimental data by more accurately modeling the dispersion terms in our interaction potential. We calculate values of α_d=5.132x10^{-4} W/(m·K^2) and β_d=2.022 W/(m·K), close to the experimental values of 5.268x10^{-4} W/(m·K^2) and 2.029 W/(m·K).[40]

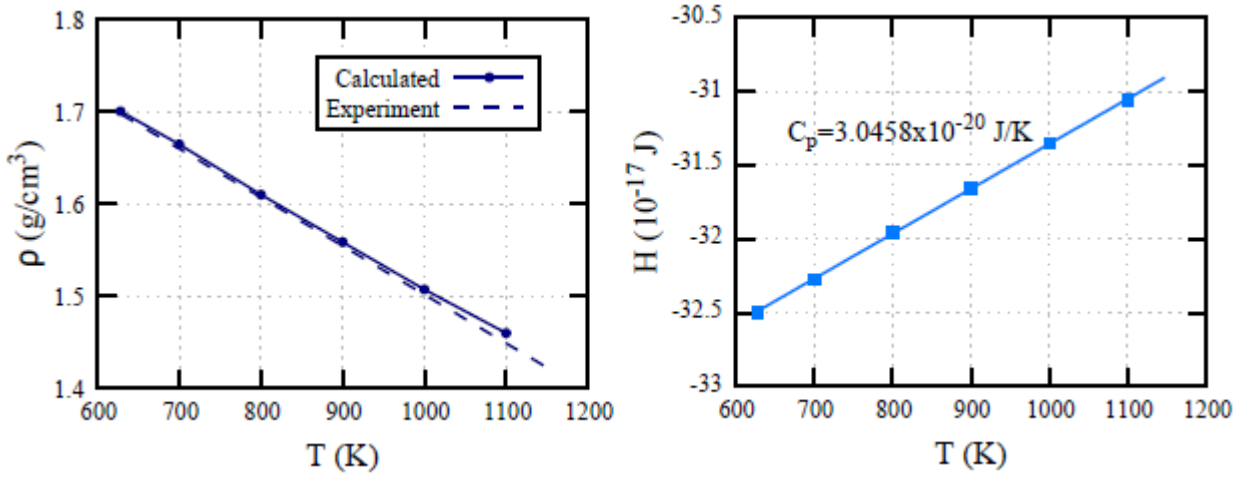

Figure 25: Density and enthalpy vs. temperature for LiCl-KCl eutectic. Our density results agree well with experimental data from Janz[40], and specific heat capacity is close to the estimated value[39].

These simulation cells have the same number of ions has those used to calculate the heat capacities for pure alkali halides, permitting direct comparison. The heat capacity for the mixture is slightly higher, probably because C_p tends to very slightly increase for molten salts at lower temperatures[30]. The specific heat capacity is calculated to be c_p=1.289 kJ/(kg·K), within 7% of the measured 1.200 kJ/(kg·K)[39]. Overall, this model seems very successful and proves that our NPT methodology holds up well when applied to multi-component mixtures.

Transport Properties

The NVT simulations performed here had a length of 5 million time steps. Both conductivities can be seen in Figure 26. We once again see the underestimation of σ at lower temperatures, and a temperature dependence that is too strong. Fit parameters of σ_0= 50.533 S/cm and E_1=38,519 J mol^{-1} were calculated. The experimental values are much different, at 23.533 S/cm and 16.356 J mol^{-1}. However, this result does show the effect of mixing on a melt's σ. Pure LiCl has a σ value which is ~2x as large at temperatures above 900K, where both salts are in liquid phase. The cause for this reduction is the introduction of the much larger K^+ ions to the melt. They have a much lower mobility, curtailing bulk flow of the cations in the melt. At 1100K, the LiCl-KCl σ value of 3.2 S/cm is closer to the KCl's value of 2.3 than LiCl's 6.7, even though 59.5% of the melt is composed of LiCl. Therefore the large K^+ ion has an effect on the electrical conductivity that is disproportionate to its concentration. This has important consequences; small amounts of impurities could have a significant impact on salt's overall ion mobility.
The calculations for λ are quite consistant, yielding values that lie somewhere between the average values of pure LiCl and KCl. Furthermore, a weak negative temperature dependence is also evident here; the line of best fit has paramteres of α_t=9.378x10^{-5} W/(m·K^2) and β_t=0.561

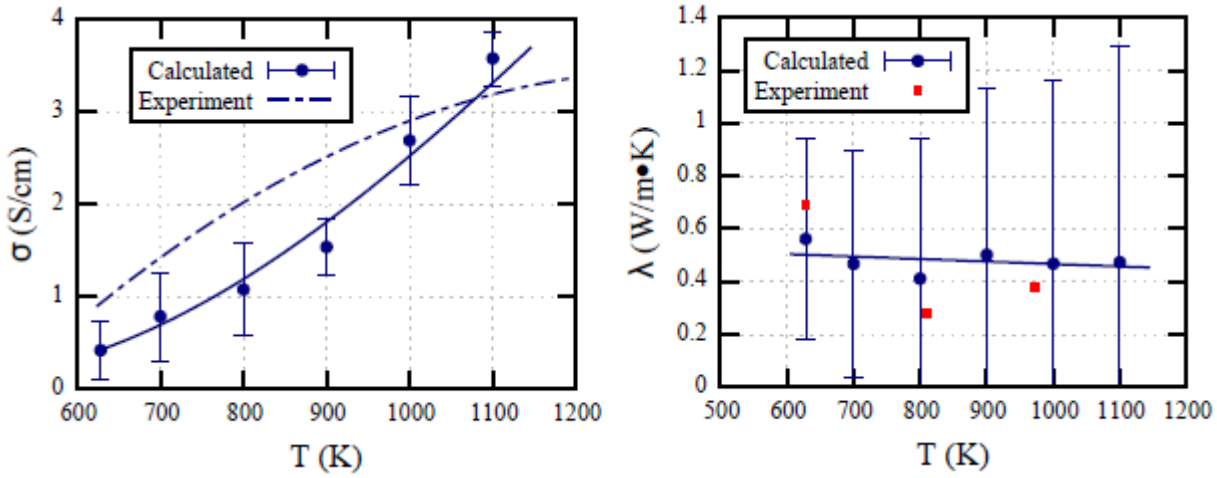

Figure 26: Conductivities of LiCl-KCl eutectic. Our calculations for σ once again underestimate experimental data[40]. The results for λ seem reasonable given the small amount of experimental data available[39]. The large error bars are because of the large amount of LiCl in the system.

W/(m·K). We have only been able to find data on this property for three individual temperature points, plotted in red. The values of these points vary widely, but all are within the statistical error of our simulation. The error bars are extremely large for two reasons. First, the calculation of λ for a three component system involves 6 Green-Kubo functions instead of the 3 required for 2 binary salts. This means we have to take errors from 3 more sources into account. Secondly, the MS contains 60% LiCl, which was shown to have the same issue of inflated statistical errors due to a cation-anion size discrepancy. The small variation of our six data points (all fall within 0.2 W/(m·K) range) leads us to believe that the statistical error is smaller than the plotted error bars, probably around 0.2 W/(m·K). This result is important for the ADSMS project; we now have estimates for the both λ and it's temperature dependence for the proposed secondary salt.

Lastly we look at the LiCl-KCl eutectic's viscosity, which is plotted in Figure 27. The

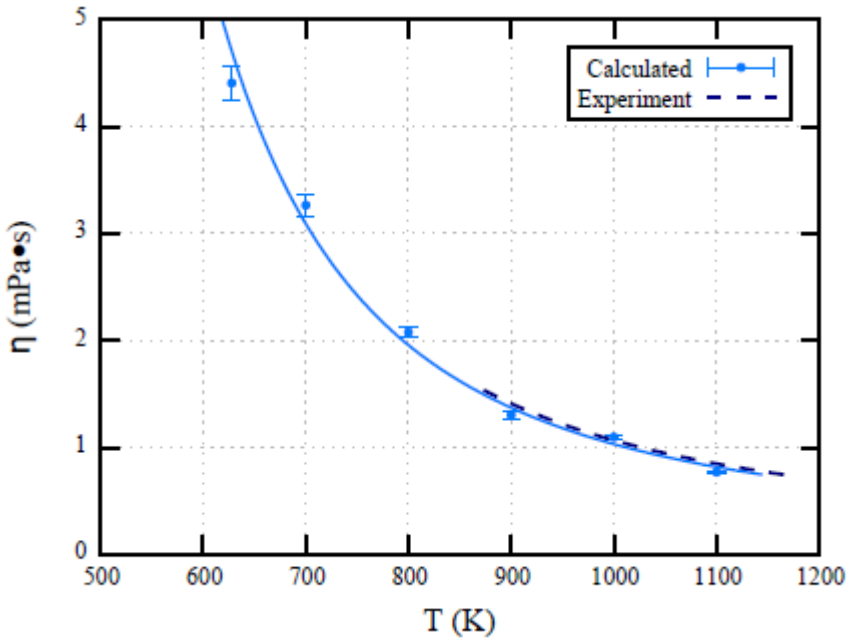

0

Figure 27: Viscosity vs. temperature for a LiCl-KCl eutectic. Agreement with experiment is excellent, showing our methodology extends to describe salt mixtures.

correlation between our values and experiment is astonishingly good, with discrepancies of less than 5%. This could be in part due to the larger gap between the experimental temperatures and the eutectic's freezing point. It is quite interesting that the viscosity of KCl was also predicted almost perfectly. Because the large K^+ ions affect ion mobility much more than the Li^-, this accuracy seems to have carried over to this mixture. The fit parameters used here were η_0=0.07986 mPa·s and E_2=21,276 J mol^{-1}, and are within 10% of the experimentally determined values of 0.0861 m·Pas and 20,926 J mol^{-1}.[39]

NaCl-UCl_3

We next study an alkali chloride - trichloride system in order to evaluate how the two different

Table 7: Summary of MD cells for NaCl-UCl_3

UCl_3 % concentration	Number of ions			ρ (g/cm^3)		η (mPa·s)	
	Na^+	U^{3+}	Cl^-	Calculated	Experiment	Calculated	Experiment
0	256	0	256	1.541	1.541	1.63	1.26
25	110	37	221	2.776	2.633	2.80	1.15
40	110	73	329	3.311	3.199	3.97	1.91
60	90	60	330	3.919	3.745	5.99	2.49
85	16	90	286	4.428	4.389	8.08	3.05
100	0	90	270	4.674	4.700	9.57	2.38

microscopic structures of these salts interact with each other. We use a NaCl-UCl_3 mixture, and we sweep the concentration of UCl_3 from 0 to 100%. We expect the mixture to act more and more like a trichloride as more UCl_3 is added, adjusting the ratio of anions to cations from 1 to 3. We do not examine the conductivities here because of a lack of experimental data. The different melt concentrations, and the number of ions in each simulation, and their densities and viscosities are tabulated in Table 7. The NPT used for this melt were run for 5 million time steps, and all runs were done at 1100K. Experimental data was taken from the work of Desyatnik[36].

Figure 28 shows the density plotted against the left axis, and the viscosity plotted against the right axis. The density of the melt is predicted quite well, with a maximum error of 5%. The calculated data seems to over predict the density more as the ratio of NaCl to UCl_3 approaches unity. We noted this effect in our mixture of LiCl-KCl eutectic as well; it is probably due to the interaction potential parameters being optimized for pure salts. It is then no surprise that the greatest error is located in the region with a 1 to 1 ratio between constituent salts.

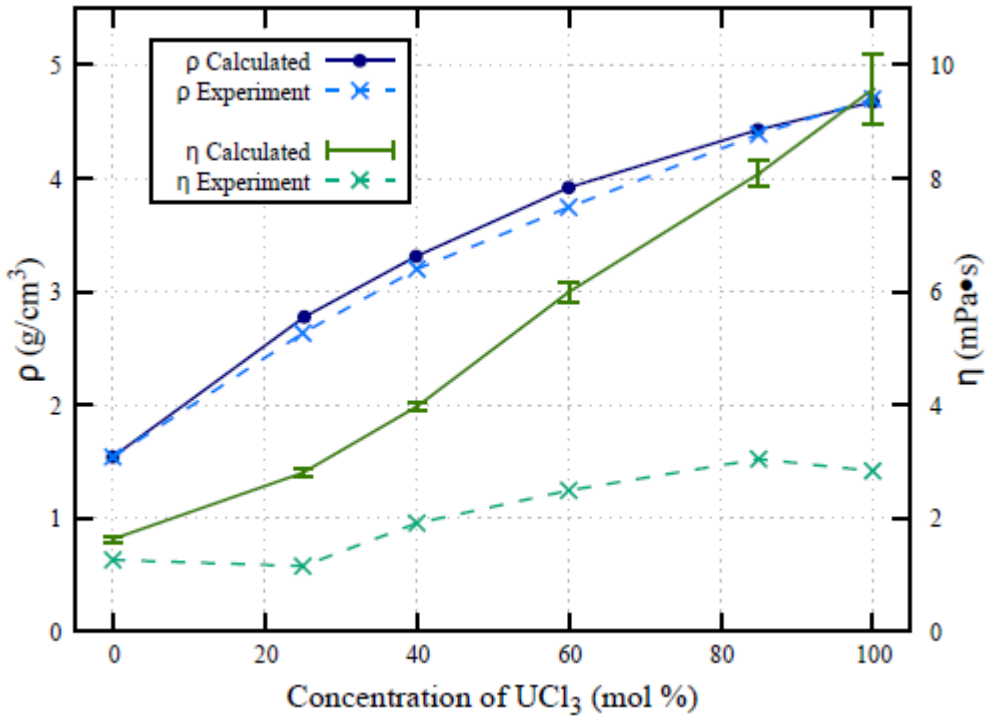

Figure 28: Density and viscosity as a function of UCl_3 concentration in a NaCl-UCl_3 melt. We are able to accurately describe the density dependence, but the viscosity is badly overestimated for high trichloride concentrations. Simulations were done at 1100K.

Our results for viscosity, on the other hand, show that our gross over estimate of pure UCl_3 viscosity at low temperatures causes the same effect to occur for all concentrations, with the magnitude of the discrepancy depending strongly on UCl_3 concentration. This effect was seen in the LiCl-KCl mixture as well; large K^+ ions lowered the viscosity of the melt closer to that of KCl. Here, the addition of large trivalent U^{3+} ions causes a lowered ionic mobility and facilitates the formation of ionic complexes, increasing the viscosity. Because our code seemed to overemphasize these effects in pure UCl_3, it does so in this melt as well.

Fuel salt ($NaCl$-$PuCl_3$-$LaCl_3$)

Having tested the performance of our interaction potential parameters and evaluated the effects of mixing various molten salts together, we now model the ADSMS fuel salt. This salt will contain a complex mixture NaCl, transuranic trichlorides, and rare earth trichlorides. Here we approximate it as a ternary $NaCl$-$PuCl_3$-$LaCl_3$ mixture, with the $PuCl_3$ representing the transuranic trichlorides and $LaCl_3$ representing all rare earth fission products. The molar composition of trichlorides is fixed to be 88 % $PuCl_3$ and 12% $LaCl_3$. We believe this is a reasonable approximation, because the TRU from SNF consists mainly of plutonium isotopes. Also, the concentration of rare earth fission products is low, so deviations caused by them being modeled as lanthanum should be small.

Density and heat capacity

During the ADSMS system's operation, transuranics will be fissioned into lighter rare earth elements, causing the ratio of TRU to NaCl to vary with time. Additionally, we would like to be able to fine-tune the fuel salt composition in order to achieve optimal neutronics. For these reasons, we calculate a density map for the fuel salt, slightly varying the ratio of trichlorides (XCL_3) to sodium chloride. This map can be seen in Figure 29, and a summary number of ions used in each simulation is shown in Table 8. We confirm that the density increases as the

Table 8: Summary of Fuel Salt Density Map Simulations

XCl_3 concentration	Number of ions				ρ (g/cm^3)	
	Na^+	La^{3+}	Pu^{3+}	Cl^-	α_d (10^{-4} g/cm^3•K)	β_d (g/cm^3)
33%	110	7	48	275	8.400	3.956
32%	110	6	46	266	8.379	3.919
31%	110	6	43	257	8.261	3.854

concentration of heavy trichlorides is increased. In fact, the densities calculated here at 1100K are very similar to those calculated in our study of a varying mixture of NaCl- UCl_3. The density decreases with increasing temperature; a relation which provides our system with an important passive safety feature. This trend is not greatly affected by slight changes in trichloride concentration. We predict a modeling overestimation by a maximum of 5% based on our previous model of a NaCl-UCl_3 mixture. Here the statistical error is assumed to be negligible when compared to the modeling error. Using this data it has been decided to use a 32% trichloride concentration in the ADSMS system; the rest of this section will examine a NaCl-$PuCl_3$-$LaCl_3$ (68,28,4%) melt.

The heat capacity of the fuel salt was also calculated and can be seen in Figure 30. The specific

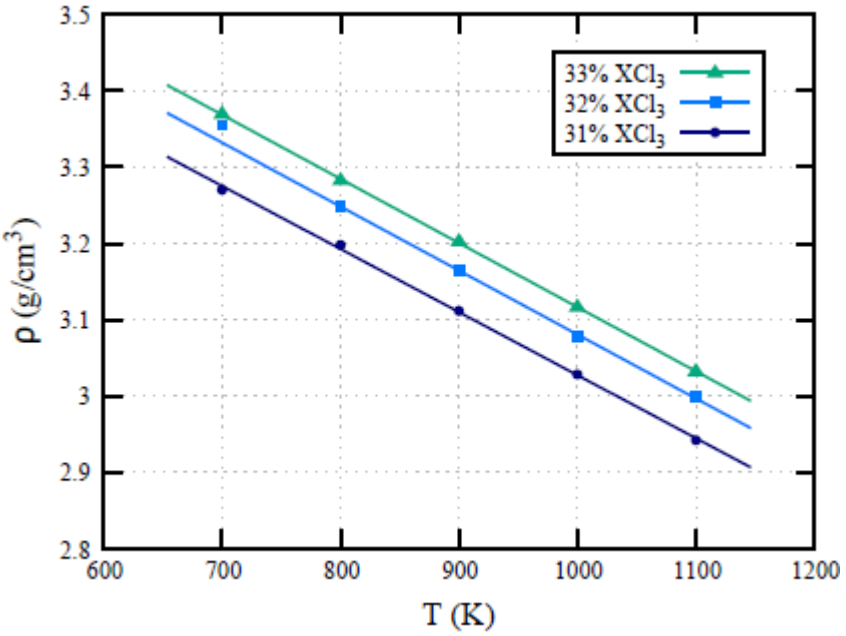

Figure 29: A density map for the NaCl-$PuCl_3$-$LaCl_3$ ADSMS fuel salt. The concentration of trichlorides (XCL_3) was slightly varied. The ratio of $PuCl_3$ to $LaCl_3$ was kept fixed at 88% and 12% of the total trichloride content.

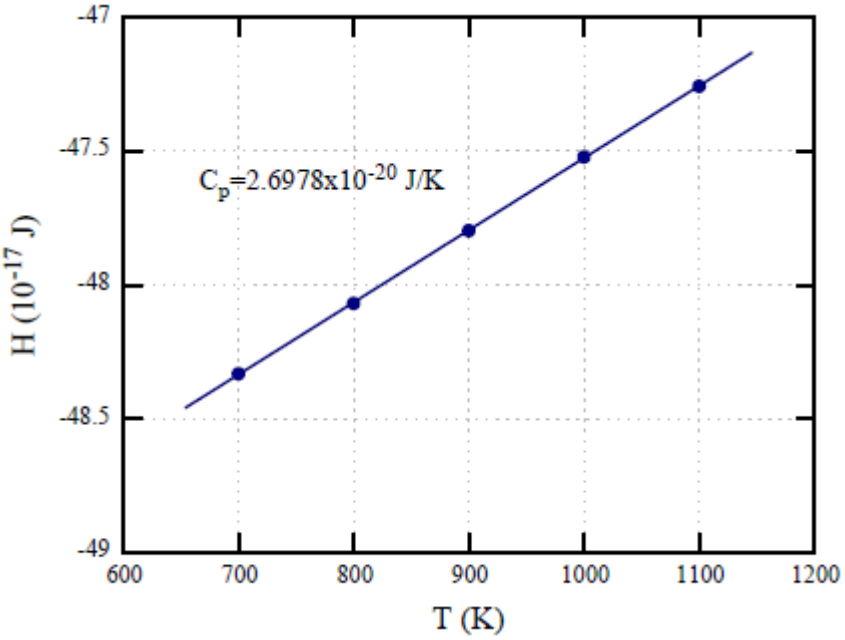

Figure 30: Heat capacity calculation for NaCl-$PuCl_3$-$LaCl_3$ (68,28,4%) fuel salt. The specific heat capacity of the melt lies between the values for pure NaCl and pure UCl_3.

heat capacity was calculated to be c_p=0.6764 kJ/(K·kg), a value that lies between those calculated for pure NaCl and UCl_3. This value is likely to be slightly larger than the actual specific heat capacity, simply because our approximations of the fuel only containing plutonium and lanthanum lower the total system's mass. However this effect is quite small compared to our estimated modeling error of 6%, a value we have determined by examining the deviations with experiment present in the other systems studied.

Transport properties

Because the fuel salt is a four component system, ten separate correlation functions must be calculated to determine the thermal conductivity of the system. This means there are ten terms contributing to the total error. In order to offset these large errors we ran the fuel salt NVT

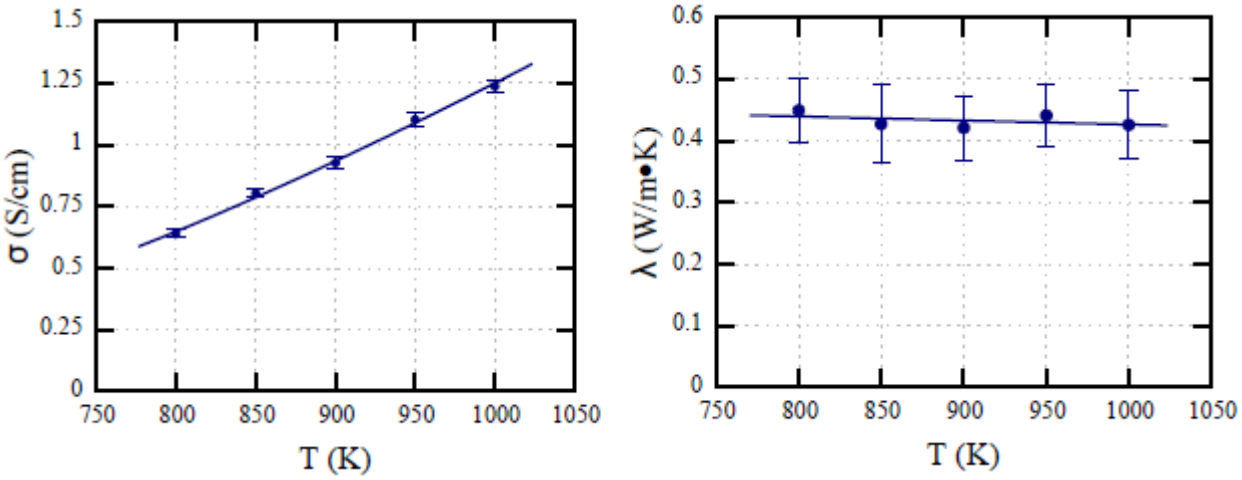

Figure 31: Simulated conductivities of NaCl-$PuCl_3$-$LaCl_3$ (68,28,4%) fuel salt. Simulations were run for twice the amount of time in order to reduce statistical errors. We expect σ to be an underestimation based on our previous results. The data for λ is very consistent and has weak temperature dependence.

simulations for 10 million time steps instead of 5, a decision which reduces our statistical errors by a factor of $\sqrt{2}$. Figure 31 shows the results of the fuel salt conductivity calculations.

We expect the electrical conductivity to be underestimated in this temperature range by anywhere from 30% to 60% based on our results for pure NaCl and $LaCl_3$ respectively. We therefore consider the values calculated here as a lower bound on σ. Our results for λ, on the other hand, have not shown any systematic deviation from experiment in past simulations. The results for the fuel salt are consistent, in the same range as other molten salts, and show a weak temperature dependence. Because the temperature variation is so small compared to the statistical error, we average all 5 points together to estimate λ = 0.43(6) W/(m·K). The error in the last digit takes the statistical error of 12% and assumes a 5% modeling error. This is perhaps our most important result; λ has a large effect on the ADSMS system's performance and was previously unknown. The fit parameters used for σ are σ_0= 17.13 S/cm and E_1=21,847 J mol^{-1},

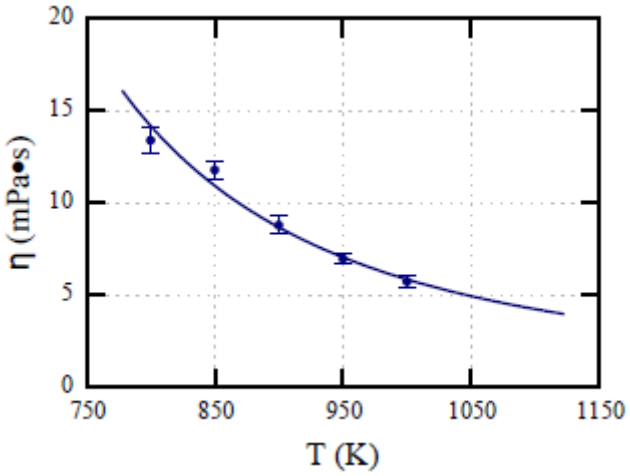

Figure 32: Simulated viscosity vs. temperature for a NaCl-$PuCl_3$-$LaCl_3$ fuel salt. We expect these values to overestimate the actual viscosity after considering our previous results for UCl_3 salts. These values therefore constitute an upper boundary on η.

and those used for λ are α_t=6.552x10^{-5} W/(m·K^2) and β_t=0.492 W/(m·K).

Finally, the simulated fuel salt viscosity is graphed in Figure 32. The fit parameters used were η_0=0.1717 mPa·s and E_2=29,356 J mol^{-1}. We expect these results to be an over prediction because our code seems to systematically exaggerate the viscosity for trichlorides. However, based on our work with a NaCl-UCl_3 system, it is expected that the deviation is not as large as those for pure trichloride systems. In fact, our value for the viscosity at 1100K is very close to the calculated value of a NaCl-UCl_3 (68,32%) system according to Figure 28. As the calculated values there were about twice as large as experiment, we speculate that our fuel salt viscosities are increased by close to a factor of 2. The results here will be useful to the ADSMS collaboration by setting an upper boundary for the fuel melt viscosity. We conclude our study by summarizing the calculated properties at the proposed bulk operational temperature of 650°C (923K).

Table 9: Summary of Calculated ADSMS Fuel Salt Properties

Property	Units	Value at 650°C	Estimated Error
ρ	g/cm^3	3.146	0.157
c_p	kJ/(K·kg)	0.676	0.041
σ	$S\ cm^{-1}$	1.00	Lower bound
λ	W/(m·K)	0.431	0.050
η	mPa·s	7.87	Upper bound

CHAPTER VI

CONCLUSIONS

We have performed molecular dynamics simulations of various chloride melts using a polarizble ion model (PIM) to accurately predict thermal, physical and transport properties of molten salt systems. The PIM is a computational experiment which simulates a system of ions and solves for each ion's equation of motion. Simulation parameters, including ensemble type, simulation length, and time step were strategically chosen to provide accurate results within a reasonable computational time. The interaction potential parameters used in the simulations were validated by comparing the microscopic structure of each salt to experimentally measured RDFs. Excellent agreement between experimental and simulated RDFs was achieved for all ionic species used in this study. The only system lacking experimental validation is $PuCl_3$: there is no experimental data for the RDF for plutonium in a chloride melt. We have compensated for this by using La^{3+} as a surrogate for Pu^{3+} and are confident in the accuracy of this first order simulation.

A framework was developed to calculate the density, heat capacity, electrical conductivity, thermal conductivity, and viscosity of molten salts. Significant use of correlation functions and Green-Kubo relations has been employed in the calculation of transport properties, but large amounts of data were required in order for the functions to converge. Our results for density and heat capacity are quite good, with maximum deviations of 5 and 7% respectively from experimental values. The calculations for thermal conductivity were also quite successful, being

within modeling error for all alkali chloride melts, and producing reasonable estimates of the ADSMS secondary and fuel salts. Errors for the thermal conductivity were typically around 10%, but became inflated when lithium was present in the melt. Additionally, larger statistical errors were present in multi-component melts, as more correlation functions had to be calculated.

Results for viscosity agreed with experiment quite well for alkali chlorides, and LiCl-KCl eutectic. Our model also correctly reproduced the correct form of temperature dependence for this value. However, we see a systematic over prediction of the viscosity in melts containing heavy trichlorides. This is probably due to changes in the microscopic structure of the melt caused by the change in cation to anion ratio. Large ionic complexes and bigger cation sizes could be reducing the ion mobility, causing the liquid to become thicker. The magnitude of the deviation from experiment seems to be linearly proportional to the concentration of trichlorides in the melt. For these reasons, we treat our calculated values for melt viscosity as an upper boundary, with the expectation that the actual salt viscosity will be somewhat lower.

Our model may not be appropriate for accurately calculating the electrical conductivities of molten salts, as we see a systematic underestimate of this value at lower temperatures. Furthermore, our model seems to treat the temperature dependence very linearly instead of the Arrhenius type. These deviations may be caused by charge current due to things other than bulk ion flow, or by nonlinear effects that arise close to the molten salt's freezing point. That said, we do believe these results provide first-order approximations for the electrical conductivity, as our calculations do get within the neighborhood of experimental values.

Finally, we have modeled the ADSMS fuel salt using a NaCl-$PuCl_3$-$LaCl_3$ model. The density was mapped for varying compositions, and a 32% trichloride concentration was chosen. Working estimates of the density, heat capacity, and thermal conductivity were produced for the ADSMS fuel salt and secondary coolant, and limits were placed on the melt's viscosity and electrical conductivity. These values will be of importance to the ADSMS collaboration as they design the ADSMS system's molten salt cores. Experiments using surrogates for plutonium, such as lanthanum, need to be done in order to confirm the values calculated here.

This work furthers the goal of the ADSMS collaboration of constructing an economic and safe device capable of destroying the world's highly radiotoxic inventory of TRU. This will be a large step forward for the nuclear industry, as it eliminates the most enduring hazard of modern nuclear power.

REFERENCES

[1] "Nuclear Share Figures, 2001-2011." World Nuclear Association, 2012 http://www.world-nuclear.org/info/nshare.html.

[2] "Transuranic Radionuclides." Argonne National Laboratory, 2005, http://www.ead.anl.gov/pub/doc/transuranics.pdf.

[3] Simpson, M. F. & Law, J. D. Nuclear Fuel Reprocessing. **INL/EXT-10-17753** (2010).

[4] Sattarov, Akhdiiyor, et al. Neutronics and Molten Salt Chemistry for Accelerator-Driven Subcritical Fission to Close the Nuclear Fuel Cycle. *Proceedings from the 2012 CAARI Conference* (2013).

[5] "Final Updated Report of the Disposal Subcommittee to the Full Commission." edited by Blue Ribbon Commission on America's Nuclear Future, 2012.

[6] Nuclear Energy Agency, JANIS Remote Database, version 32, 2012.

[7] Holcomb, D. E. *et al*. Fast Spectrum Molten Salt Reactor Options. **ORNL/TM - 2011 / 105** (2011).

[8] Mourogov, A. & Bokov, P. M. Potentialities of the fast spectrum molten salt reactor concept: REBUS-3700. *Energy Conv. Manag.* **47**, 2761-2771 (2006).

[9] Sooby, E. et al. Candidate Molten Salt Investigation for an Accelerator Driven Subcritical Core. J. Nucl. Mater. Submitted for Publication Oct. 2012, Accepted March 2013.

[10] Williams, D. F. "Molten Salt Coolants for the NGNP/NHI Heat-Transfer Loop." edited by U.S. Department of Energy, 2006.

[11] www.comsol.com, (2013).

[12] Frenkel, D. & Smit, B. in *Understanding Molecular Simulation: from algorithms to applications* (San Diego : Academic Press, San Diego, 1996).

[13] Madden, P. & Wilson, M. 'Covalent' effects in 'ionic' liquids. *J. Phys.- Condes. Matter* **12**, A95-A108 (2000).

[14] Zhang, S. & Chen, N. Ab initio interionic potentials for NaCl by multiple lattice inversion. *Phys. Rev. B* **66**, 064106 (2002).

[15] Rollet, A. & Salanne, M. Studies of the local structures of molten metal halides. Annu. Rep. Prog. Chem., Sect. C, 2011, 107, 88–123

[16] Baierlein, R. in *Thermal Physics*. (New York: Cambridge University Press, 1999.)

[17] Hansen, P. & McDonald, I. in *Theory of Simple Liquids*. (New York: Academic Press, 1976.)

[18] Salanne, M. et al. Thermal conductivity of ionic systems from equilibrium molecular dynamics. *J. Phys.- Condes. Matter* **23**, 102101 (2011).

[19] Madden, P. & Wilson, M. Polarization Effects in Ionic Systems from 1st Principles. *J. Phys - Condes. Matter* **5**, 2687-2706 (1993).

[20] Madden, P. & Wilson, M. 'Covalent' effects in 'ionic' systems. *Chem. Soc. Rev.* **25**, 339-(1996).

[21] Ohtori, N., Salanne, M., & Madden, P. Calculations of the thermal conductivities of ionic materials by simulation with polarizable interaction potentials. J. Chem. Phys. **130**, 104507 (2009).

[22] Salanne, M. et al. Calculation of Activities of Ions in Molten Salts with Potential Application to the Pyroprocessing of Nuclear Waste. *J Phys Chem B* **112**, 1177-1183 (2008).

[23] Tazi, S. *et al*. A transferable ab initio based force field for aqueous ions. *J. Chem. Phys.* **136**, 114507 (2012).

[24] Masset, P. et al. Thermochemical properties of lanthanides (Ln = La, Nd) and actinides (An = U, Np, Pu, Am) in the molten LiCl–KCl eutectic. *J. Nucl. Mater*., **344**, 173-179 (2005).

[25] K. Fukasawa, et al. Thermodynamic properties of trivalent lanthanide and actinide ions in molten mixtures of LiCl and KCl. *J. Nucl. Mater.*, **424**, 17-22 (2012).

[26] Andersen, H. Molecular-Dynamics Simulations at Constant Pressure And-Or Temperature. *J. Chem. Phys.* **72**, 2384-2393 (1980).

[27] Okada, I. et al. Structural Determination of a Molten (Li-K)Cl Mixture of the Eutectic Composition by X-Ray-Diffraction and Molecular-Dynamics Simulation. *Chem. Phys. Lett.* **100**, 436-441 (1983).

[28] Janz, G. J. et al. *Molten salts. Volume 1, Electrical conductance, density, and viscosity data* (United States Dept. of Commerce, National Bureau of Standards, 1968)

[29] Edwards, F. et al. The structure of molten sodium chloride. *Journal of Physics C: Solid State Physics* **8**, 3483 (1975).

[30] Chase, M. W. & National Institute of Standards and Technology (U.S.). in *NIST-JANAF thermochemical tables* (American Institute of Physics for the National Institute of Standards and Technology, Woodbury, N.Y., 1998).

[31] Nagasaka, Y., Nakazawa, N. & Nagashima, A. Experimental-Determination of the Thermal-Diffusivity of Molten Alkali-Halides by the Forced Rayleigh-Scattering Method .1. Molten LiCl, NaCl, KCl, RbCl, and CsCl. *Int. J. Thermophys.* **13**, 555-574 (1992).

[32] Ohtori, N., Oono, T. & Takase, K. Thermal conductivity of molten alkali halides: Temperature and density dependence. *J. Chem. Phys.* **130**, 044505 (2009).

[33] Redkin, A. et al. The electrical conductivity of chloride melts. *Ionics* **18**, 255-265 (2012).

[34] Okamoto, Y., Hayashi, H. & Ogawa, T. X-ray diffraction analysis of molten trivalent halides. *Jpn. J. Appl. Phys. Part 1 - Regul. Pap. Brief Commun. Rev. Pap.* **38**, 156-159 (1999).

[35] Okamoto, Y., Madden, P. & Minato, K. X-ray diffraction and molecular dynamics simulation studies of molten uranium chloride. *J. Nucl. Mater.* **344**, 109-114 (2005).

[36] Desyatnik, V. et al. Density, Surface-Tension, and Viscosity of Uranium Trichloride Sodium Chloride Melts. *Soviet Atomic Energy* **39**, 649-651 (1975).

[37] Dworkin, A. & Bredig, M. Heats of Fusion and Transition of Alkaline Earth and Rare Earth Metal Halides. *J. Phys. Chem.* **67**, 697-& (1963).

[38] Potapov, A. & Sato, Y. Viscosity of Molten Rare Earth Metal Trichlorides II. Cerium Subgroup. *Z. Naturfors. Sect. A-J. Phys. Sci.* **66**, 649-655 (2011).

[39] Williams, D. F. Assessment of Candidate Molten Salt Coolants for the NGNP/NHI Heat-Transfer Loop. **ORNL/TM-2006/69** (2006).

[40] Janz, G. J. *et al*. Molten salts: Volume 4, part 2, chlorides and mixtures---electrical conductance, density, viscosity, and surface tension data. *J. Phys. Chem. Ref. Data* **4**, 871-1178 (1975).

[41] Sindzingre, P. & Gillan, M. Computer-Simulation Study of Transport-Coefficients in Alkali-Halides. *J. Phys.-Condes. Matter* **2**, 7033-7042 (1990).

[42] Lee, J. F. in *Statistical thermodynamics* (Reading, Mass., Addison-Wesley Pub. Co, Reading, Mass., 1973).

[43] de Groot, S. in *Thermodynamics of irreversible processes* (Amsterdam, North-holland Pub.Co.; New York, Interscience Publishers, 1951).

[44] Galamba, N., de Castro, C. & Ely, J. Thermal conductivity of molten alkali halides from equilibrium molecular dynamics simulations. *J. Chem. Phys.* **120**, 8676-8682 (2004).

[45] Salanne, M. *et al*. Transport in molten LiF-NaF-ZrF4 mixtures: A combined computational and experimental approach. *J. Fluorine Chem.* **130**, 61-66 (2009).

[46] Alfe, D. & Gillan, M. First-principles calculation of transport coefficients. *Phys. Rev. Lett.* **81**, 5161-5164 (1998).

APPENDIX A

FORMULAS USED FOR MULTI-COMPONENT SYSTEMS

In chapter II we derived the Green-Kubo formula for a one-component ionic liquid's diffusion coefficient. We then went on to state similar expressions for other various transport properties. These expressions are significantly more complex for ionic liquids containing multiple components. First, imbalances in different ion concentrations may cause internal electrostatic potentials not present in one-component liquids. Secondly, differing ion concentrations lead to chemical potentials that give rise to internal diffusion of ions. These two factors combine to form electrochemical potentials, which alter the motion of each of the liquid's components differently. Furthermore, these potentials can coexist with a temperature gradient. Thus, the dynamics of the liquid are based on multiple thermodynamic forces: the temperature gradient, ∇T, the electrostatic potential difference, $\nabla\phi$, and the chemical potential gradients, $\nabla\mu_i$.

In the following treatment, the following notation is used for Green-Kubo relations:

$$L_{ab} = \frac{1}{3k_B V}\int_0^\infty d\tau \, \langle j_a(\tau)\cdot j_b(0)\rangle. \qquad \text{(A1)}$$

j_e is the system's microscopic energy current, j_c is the net microscopic charge current, and j_n indicates the charge current of the nth ionic species.

Conductivities of binary systems

Consider an ionic liquid containing two types of ions, one being a cation with charge $z_1$and the other an anion of charge z_2. Because of the relative concentrations of the ions in the liquid two chemical potentials μ_1 and μ_2 will be present. For simplicity we first combine these potentials with any electric potential, ϕ, present in the liquid to form the electrochemical potentials $\tilde{\mu}_n=\mu_n+z_n\phi$. Furthermore, we can redefine electrochemical potential of the anionic species as zero as long as we shift the other potential with the relation

$$\acute{\mu}_1=\frac{\tilde{\mu}_1-\tilde{\mu}_2}{z_1-z_2}. \tag{A2}$$

This manipulation is advantageous because it is now possible to relate the macroscopic energy and charge fluxes, J_E and J_1 respectively, to the thermal driving force, $X_E=-\nabla T$, and the electrochemical driving force, $X_1=-T\nabla(\acute{\mu}_1/T)$. Furthermore, the coefficients of these phenomenological equations are Green-Kubo relations which can be calculated directly from MD simulations[18,41]:

$$J_E=\frac{1}{T^2}(L_{EE}X_E+L_{E1}X_1) \tag{A3}$$

$$J_1=\frac{1}{T^2}(L_{1E}X_E+L_{11}X_1). \tag{A4}$$

J_E and J_1 are a set of conjugate flows for these thermodynamic driving forces, meaning they obey the Onsager reciprocal relation[42,43]:

$$L_{ab}=L_{ba} \tag{A5}$$

Equations (A4) and (A5) can be used to eliminate X_1 and L_{1E} from (A3), yielding

$$J_E = \frac{X_E}{T^2}\left(L_{EE} - \frac{L_{E1}^2}{L_{11}}\right) + \frac{L_{E1}}{L_{11}} J_1. \quad \text{(A6)}$$

In the absence of electrical current, so that $J_1=0$, (A6) has the form of Fourier's Law of heat conduction with the λ of the binary ionic liquid being[44]

$$\lambda = \frac{1}{T^2}\left(L_{EE} - \frac{L_{E1}^2}{L_{11}}\right). \quad \text{(A7)}$$

It can also be shown that the electrical conductivity is given by the formula [21,41]:

$$\sigma = \frac{L_{cc}}{T}. \quad \text{(A8)}$$

This reproduces our result for a one-component ionic liquid.

Conductivities of multi-component systems

Now consider a liquid containing N different ionic species. For our purposes, we assume that the species labeled 1 through N-1 are cations, and the Nth species is an anion, such as Cl^-. In general, the energy and N-1 species charge currents are related by a system of N equations [18]:

$$J_E = \frac{1}{T^2}\left(L_{EE} X_E + \sum_j^{N-1} L_{Ej} X_j \right) \quad \text{(A9)}$$

$$J_i = \frac{1}{T^2}\left(L_{iE} X_E + \sum_j^{N-1} L_{ij} X_j \right). \quad \text{(A10)}$$

Here the index i runs from 1 to N-1. To calculate the λ, we assume there is no electrical current, so each $J_i=0$. Then the equations (A10) can be solved to give each X_j in terms of X_E. Substitution of these expressions into (A9) relates J_E to X_E.

For example, in a three-component system (A10) will reduce to the relations

$$X_1 = \frac{L_{12}L_{E2} - L_{E1}L_{22}}{L_{11}L_{22} - L_{12}^2} X_E \tag{A11}$$

$$X_2 = \frac{L_{11}L_{E2} - L_{E1}L_{12}}{L_{12}^2 - L_{11}L_{22}} X_E. \tag{A12}$$

Substituting into (A9) yields the formula for three-component system's λ[18]:

$$\lambda = \frac{1}{T^2}\left(L_{EE} - \frac{L_{E1}^2 L_{22} + L_{E2}^2 L_{11} - 2L_{E1}L_{E2}L_{12}}{L_{11}L_{22} - L_{12}^2}\right). \tag{A13}$$

Equations (A5), (A9), and (A10) can be solved to give a general solution for the λ of an N+1 component system:

$$\lambda = \frac{1}{T^2} \frac{\begin{vmatrix} L_{EE} & L_{E1} & \dots & L_{EN} \\ L_{E1} & L_{11} & \dots & L_{1N} \\ \vdots & \vdots & \ddots & \vdots \\ L_{EN} & L_{1N} & \dots & L_{NN} \end{vmatrix}}{\begin{vmatrix} L_{11} & \cdots & L_{1N} \\ \vdots & \ddots & \vdots \\ L_{1N} & \cdots & L_{NN} \end{vmatrix}}. \tag{A14}$$

Using this approach, the λ for a four-component system is calculated to be

$$\lambda = \frac{1}{T^2}\left(L_{EE} - \frac{A}{B}\right) \tag{A15}$$

where

$$\begin{aligned} A = {} & L_{E1}^2(L_{22}L_{33} - L_{23}^2) + L_{E2}^2(L_{11}L_{33} - L_{13}^2) + L_{E3}^2(L_{11}L_{22} - L_{12}^2) \\ & + 2L_{E1}L_{E2}(L_{13}L_{23} - L_{12}L_{33}) + 2L_{E2}L_{E3}(L_{12}L_{13} - L_{11}L_{23}) \\ & + 2L_{E1}L_{E3}(L_{12}L_{23} - L_{13}L_{22}) \end{aligned} \tag{A16}$$

$$B = L_{11}L_{22}L_{33} + 2L_{12}L_{13}L_{23} - L_{12}^2L_{33} - L_{13}^2L_{22} - L_{23}^2L_{11}. \tag{A17}$$

Finally, we remark equation (A8) is true in general for multi-component systems[45].

Viscosity averaging

While equation (19) is accurate for describing the viscosity of a multi-component system, we can take advantage of the isotropy of a MS in order to increase the accuracy of the calculated value. Because a MS is homogenous is all directions, each of the three shear terms of the stress tensor, σ_{xy}, σ_{yz}, and σ_{xz}, as well as two more independent terms, $\frac{1}{2}(\sigma_{xx}\text{-}\sigma_{yy})$ and $\frac{1}{2}(\sigma_{yy}\text{-}\sigma_{zz})$, should give the same value if used for the autocorrelation function in (19)[46]. Therefore, averaging over these five values quintuples the amount of data for viscosity produced by one MD simulation. After averaging, equation (19) becomes

$$\eta = \frac{1}{5k_B VT}\int_0^\infty \langle\sigma_{xy}(\tau)\sigma_{xy}(0)\rangle + \langle\sigma_{yz}(\tau)\sigma_{yz}(0)\rangle + \langle\sigma_{xz}(\tau)\sigma_{xz}(0)\rangle + \frac{1}{4}\langle(\sigma_{xx}(\tau)\text{-}\sigma_{yy}(\tau))(\sigma_{xx}(0)\text{-}\sigma_{yy}(0))\rangle + \frac{1}{4}\langle(\sigma_{yy}(\tau)\text{-}\sigma_{zz}(\tau))(\sigma_{yy}(0)\text{-}\sigma_{zz}(0))\rangle\, d\tau. \quad \text{(A18)}$$

This extra averaging is necessary because viscosity autocorrelation functions converge very slowly, causing a large amount of data to be needed for accurate calculations.